ABSTRACT

ANALYSIS OF 3D PRINTED NdFeB POLYMER BONDED AND ORGANIC BASED MAGNETS

by

Chimaobi Ibeh

Additive manufacturing (AM), or commonly known as 3D printing, has introduced to the manufacturing and commercial sectors novel ways of reducing production times, decreasing material waste, and enabling end products with multi-material configuration and complex geometric designs. From industrial scale to customer-based printers, AM has revolutionized the approach to manufacturing, prototyping, and designing in the field of medical, automotive, aerospace, biomedical, electronics and customizable products. Recently, additive manufacturing has crossed over to the area of applications in magnetism due to the economic push for the miniaturization of electronic and mechanical devices, reduction in production costs and material & design flexibility.

The goal of this research is to add to the groundwork for the additive manufacturing with NdFeB bonded and organic based magnetic materials. Development of 3D printing methods will open doors to new applications in magnetism and will lead to significant opportunities in its applications. NdFeB bonded composites and organic based magnetic materials will be converted to feedstock and implemented into the 3D printer to fabricate magnetic objects with complex and unique shapes. The molecular, electronic and structural properties of these materials will be characterized using various analytical and physical methods and the results will be compared.

ANALYSIS OF 3D PRINTED NdFeB POLYMER BONDED AND ORGANIC BASED MAGNETS

by
Chimaobi Ibeh

A Thesis
Submitted to the Faculty of
New Jersey Institute of Technology
in Partial Fulfillment of the Requirements for the Degree of
Master of Science in Materials Science and Engineering

Department of Materials Science and Engineering

December 2018

APPROVAL PAGE

ANALYSIS OF 3D PRINTED NdFeB POLYMER BONDED AND ORGANIC BASED MAGNETS

Chimaobi Ibeh

Dr. Nuggehalli M Ravindra, Dissertation Advisor — Date
Professor, Department of Physics, New Jersey Institute of Technology

---

Dr. Sagnik Basuray, Committee Member — Date
Assistant Professor, Chemical and Materials Engineering, New Jersey Institute of Technology

---

Dr. Michael Jaffe, Committee Member — Date
Research Professor, Biomedical Engineering, New Jersey Institute of Technology

BIOGRAPHICAL SKETCH

Author: Chimaobi Ibeh

Degree: Master of Science

Date: December 17, 2018

Undergraduate and Graduate Education:

- Master of Science in Material Science and Engineering
  New Jersey Institute of Technology, Newark, NJ, 2018

- Bachelor of Science in Material Science and Engineering,
  Penn State University, University Park, Pa, 2011

Major: Material Science and Engineering

Presentations and Publications:

Magnetic Polymers: Case Studies, Chimaobi Ibeh and N.M. Ravindra (In preparation).

ACKNOWLEDGMENTS

Conducting the research and experimentation on 3D printed polymer-bonded NdFeB magnets TCNQ and HOPG magnets has been quite a learning and enduring experience. I send a big special thanks to my research advisor, Dr. N.M. Ravindra, for the mentoring and the effort in gathering up all the materials and equipment together from around the world to make this thesis possible. His relentless drive to create something out of nothing just for my success is inspiring and is a quality I'd like to possess. I thank Sam Gatley for giving me the basic understanding of 3D printing and for the engaging conversations about the entire field. He was always there to answer my questions, as well as help me with 3D printer troubleshooting and give me the confidence to finish up my thesis. I send a special thanks to my parents, brothers and sisters for the motivation to pursue a master's degree at NJIT and the encouragement to succeed. Support also came from my professors, Dr. Michael Jaffe, Dr. Sagnik Bassuray, classmates and friends, who on many levels propelled me to reach to new heights of academia. Lastly, I want to give a big and special thanks to my girlfriend, Brandice Peltier, for understanding and staying with me through the struggles of graduate school. She was always there to give me helpful advice about school, life and success. I thank NJIT for this great path of learning and success in receiving my master's degree in Material Science and Engineering.

TABLE OF CONTENTS

TABLE OF CONTENTS

(Continued)

TABLE OF CONTENTS

(Continued)

Chapter **Page**

LIST OF TABLES

Table **Page**

LIST OF FIGURES

Figure **Page**

CHAPTER 1

INTRODUCTION

1.1 Motivation

Currently, most countries around the world are heading towards good economic, technological and social standing. This global progress, however, can have a negative effect on the world's ecological system, natural energy resources and current political landscape. Pollution, depletion of nonrenewable resource, and global competition of limited energy resource have pushed the adaption for innovative energy efficiency methods and alternate energy sources. Functional magnetic materials such as advanced hard and soft magnets, magnetic refrigerants, magnetic MEMS (microelectromechanical systems), magnetic shape memory alloys, and magnetorheological fluids and elastomers, can have a substantial impact on the improvement energy efficiency of technologies (Oliver Gutfleisch, 2011). Telecommunications devices, electric motors, electronic devices and machinery have taken advantage overtime the advances of magnetic materials to become more energy efficient or creating new types of energy sources. Recent research studies have made magnets the future candidates for new sensor and actuator applications, electric motors and smart materials/systems.

Modern society takes for granted the constant electrical supply produced from the power stations, through the powerlines and into our homes. We use electricity for lighting, heating, cooling, refrigeration, electronics, machinery and transportation. In the United States, the industrial sector uses about 30% of the nation's electrical usage with 65%

consumed by electric motor technologies alone. Just taking the initiative to increase the energy efficiency would drastically decrease the overall energy cost and CO_2 emissions. Around the country, major infrastructure upgrades for generation, transmission, and distribution of electric power are needed as the general population grows and live in or nearby urban areas. The chart (Fig. 1.1) illustrates, from the year 1949 to now, the annual electric losses have outpaced the annual increase in residential electricity consumption. (Pickard and Mauri 2002, Gutfleisch, Willard et al. 2011). These issues need to be addressed with energy efficiency methods that rely on the conversion of solar, wind, ocean, hydropower, biomass, and geothermal energy into electric power.

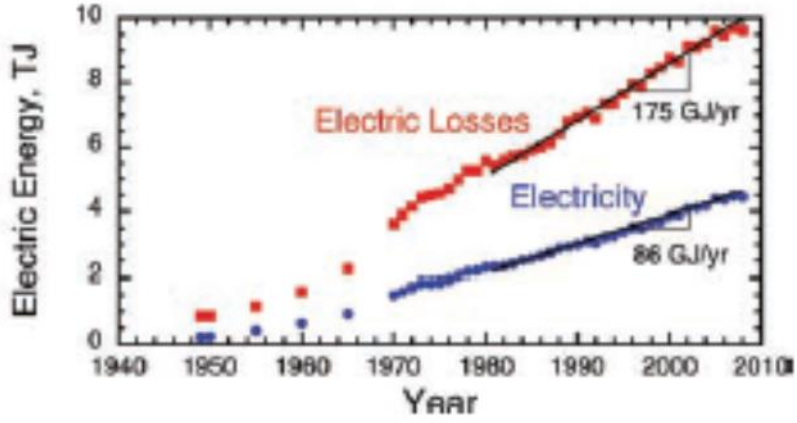

Figure 1.1 Residential electricity consumption since 1949. Electric losses include generation, transmission, and distribution.

Source: Oliver Gutfleisch, M. A. W., Ekkes Brück, Christina H. Chen, S. G. Sankar, and J. Ping Liu (2011). "Magnetic Materials and Devices for the 21st Century: Stronger, Lighter, and More Energy Efficient." Advanced Materials (23): 821-842.

The improvement of permanent magnets (PM) have shown the ability to slow down the energy consumption and increase energy efficiency. PM with the combination of the advancements of semiconductor electronics such as MOSFET (metal oxide semiconductor field effect transistors) and IGBT (insulated gate bipolar transistors) have brought

innovation to the electric motors, power electronics and intelligent controllers. Wind power has become the fastest growing sector in renewable energy generation because of the replacement of conventional generators with the PM generators that have higher operating efficiency, higher torque density and lower maintenance cost. Hybrid-electric and electric cars over time are replacing the induction motor with PM motors because of its compact size, high energy efficiency, light weight, and high torque. It's the improvement of a key PM parameter, energy product, from discovery of magnetic materials such as SmCo and NdFeB, that have increased energy efficiency as shown below.

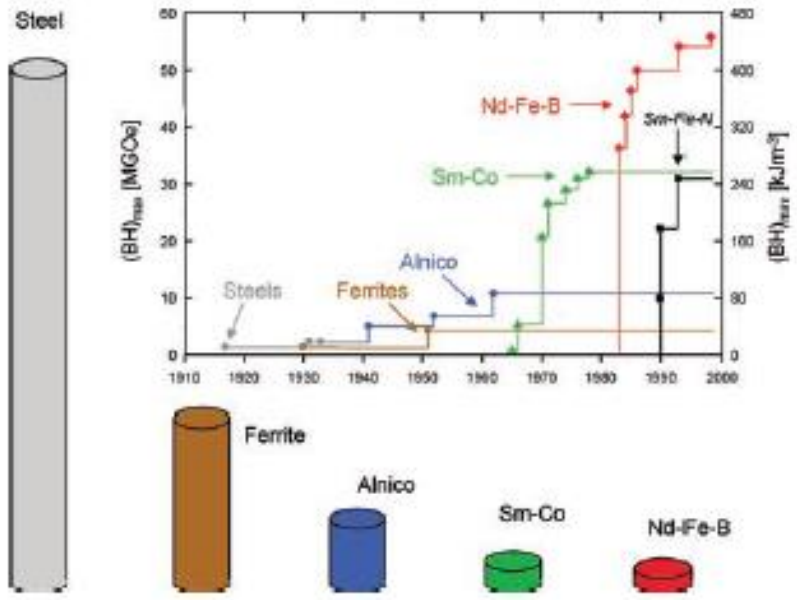

Figure 1.2 Development in the energy density ((BH) max) of the common hard magnetic materials over the years.

Source: Oliver Gutfleisch , M. A. W., Ekkes Brück , Christina H. Chen , S. G. Sankar , and J. Ping Liu (2011). "Magnetic Materials and Devices for the 21st Century: Stronger, Lighter, and More Energy Efficient." Advanced Materials (23): 821-842.

One problem with advanced PM materials is the heavy reliance on the finite supply of rare earth (RE) minerals. RE elements, which the Japanese refer to as "the seeds of technology" and to the US Department of Energy as "technology metals", are extremely

important and the foundation of this technological era. They can be found in florescent light bulbs, hybrid electric vehicles, nickel metal hydride batteries, computer hard drives, glass additives, polishing powders, direct-drive high power wind generators, speakers, nuclear fuels, radar, and most weapons systems. (Dent et al., 2011). They are the set of seventeen chemical elements shown in the periodic table below (Fig. 1.3), specifically the fifteen lanthanides and two transition metals (scandium and yttrium). The iPhone alone contains eight different RE elements; embedded in the colored screen, speakers, and the phone's circuitry.

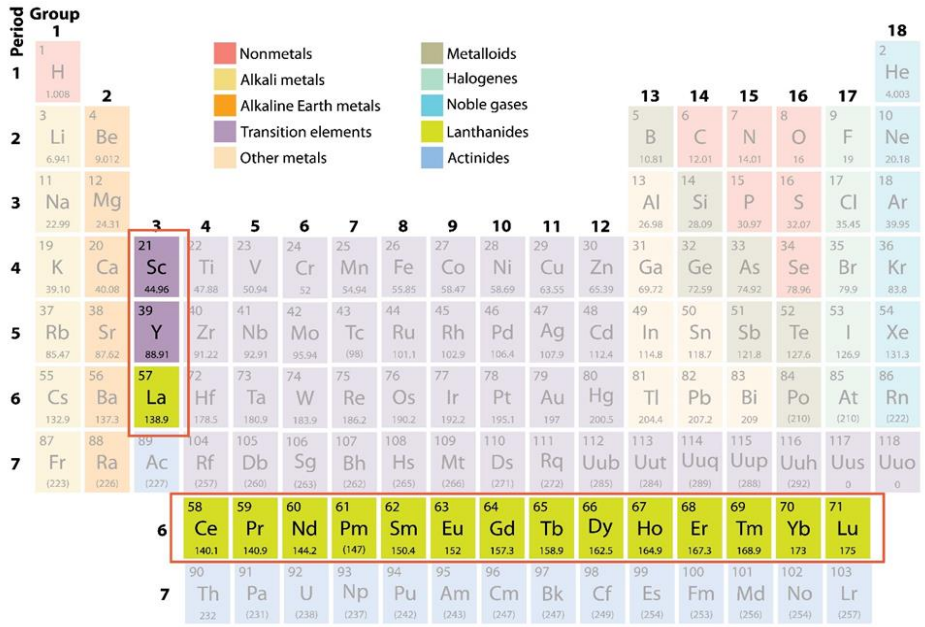

Figure 1.3 Periodic table highlighting the rare earth minerals.

Source: Oliver Gutfleisch , M. A. W., Ekkes Brück , Christina H. Chen , S. G. Sankar , and J. Ping Liu (2011). "Magnetic Materials and Devices for the 21st Century: Stronger, Lighter, and More Energy Efficient." Advanced Materials (23): 821-842.

China, world's dominant producer of RE, have a unique geological position of many large earth deposits of rare earth elements, platinum group elements, rare metals, and phosphorus. This give them the competitive edge on price and supply control over many

valuable resources. The strongest PM available, $Nd_2Fe_{14}B$, occupies 2/3 of the PM market but cost 25 times as the much easy to obtain and produced hard ferrites ($BaFe_{12}O_{19}$). Rich rare earth deposits in the Fujian, Guangdong, Jiangxi, and Sichuan regions brought out by Chinese private companies and mining corporation, allowing China step into the major role in the world market during the mid-1980s (Morrison et al., 2011). In the 1990s, the Chinese government allowed the production of RE elements with little to no regulation, which let companies set the prices low and out-compete nearly all western RE mining operations. By the year 2000, China has nearly monopolized the world's rare earth element production and own most of the world's rare earth reserve base (Morrison, 2012). With no domestic production of RE magnetic materials market, Western nations have developed current strategies to diversify the critical materials supply, lower manufacturing cost of permanent magnet and cutdown the RE supply by developing new magnetic materials.

Polymer bonded magnet, composite with permanent magnetic powder embedded into a non-magnetic matrix, was already becoming the popular replacement for pure permanent magnets. Common processing techniques used to produce bonded magnet, such as injection molding and calendaring, were less energy intensive, more environmentally safe and didn't require lengthy and costly metallurgical process. These composites were fabricated into different complex shapes and placed into many new applications. A disadvantage of the nonmagnetic binder was lowering of the overall density and diluting the magnetic properties of the powder, causing the generation of magnetic energy output per unit volume to be less than fully dense magnets.

Another alternative route away from the heavy use of rare earth elements is the minimization of waste during magnet production by applying near net-shape (NNS) manufacturing technique. NNS processes aim to create semi-finished products that are as close as possible to the desired final geometry and technological characteristics. Additive manufacturing (AM), a relatively new fabrication method for magnetic materials, makes manufacturing of net-shape easier and use of critical RE materials more efficient. (Popov, 2018) Many AM methods such as Fused Deposition Modeling, Big Area Additive Manufacturing and Stereolithography have been applied to the production of magnets creating complex and intricate shapes with enhance its magnetic properties and reduce production waste.

A new class of magnetic materials have emerged recently from molecules that have unique properties like low density, low temperature processing, coupling of magnetic ordering with other material properties and electrical insulation. These molecule/organic based magnets also have magnetic properties comparable to the traditional atomic based magnets. The simple fabrications processes for these novel materials such as chemical vapor depositions and electrodeposition are able to create materials with magnetic ordering at room temperature.

Spintronics is one area of magnetic applications that have shown interest in organic based magnetic materials. Spintronics, or spin electronics, exploits the magnetic degree of freedom of atomic electrons for information processing. Today's electronics uses tiny electrical charges to pass through the circuits. Organic based materials such as vadium-tertacyanoethylene has the potential to utilize electron spins for energy efficient and faster

information processing. New applications, such as photocontollable magnetism will have interesting impact in the near future.

The objective of this research paper is to apply the latest additive manufacturing with organic based magnetic materials to understand the physical, mechanical and magnetic properties.

CHAPTER 2

BACKGROUND AND LITERATURE REVIEW

2.1 Background Review

2.1.1 Historical Development of Magnetism

Since the beginning of time, people have developed wild theories and postulation about the mystery of lodestones that possess attractive/repulsion force on certain metals. These stones are now known to contain iron oxide (Fe_3O_4) that were magnetized by lightning strikes. Observers of magnetism during ancient times knew that some type of field that exert force permeate from or into a plain object and doesn't require continual expenditure of energy. Ingenious ideas from map surveying to perpetual motion machines were created because of this phenomenon.

2^{nd} century BC, during the Han Dynasty, devices equipped with a needle shaped lodestone, were being produce for navigation and orientation positioning. The invention quickly increased the rate of sea voyages throughout the world, accelerate growth of the global economy and human population. Fast forward to the year 1600, William Gilbert published De Magnete, a comprehensive view of the nature of magnetism which gave people a better understanding of the science phenomenon. In 1743, Daniel Bernoulli, invented the iconic iron horseshoe magnet to avoid the common problem of magnets at that time have of becoming demagnetized by its own demagnetizing field, H_d. For a uniformly magnetized ellipsoid with magnetization (M)

$$H_d = -NM \quad (1)$$

The demagnetizing field depends on the shape of the sample and the direction of magnetization. N represents the demagnetizing factor which is related to the shape and takes the value between 0 and 1. A magnet shaped like sphere has a N value of 1/3 (Fig. 1.3). A magnetized long needle has a N value of 0 when magnetized along its axis and a 1 as a thin film magnetized perpendicular to the plane. (Coey 2011). Hard steels used during those time, with the magnetization of 1.5 MA m^{-1} and coercivity H_c of no more than 30 kA m^{-1} could only retain their magnetization if D < 0.02. This is why the horseshoe and bar shapes were the only options at that time.

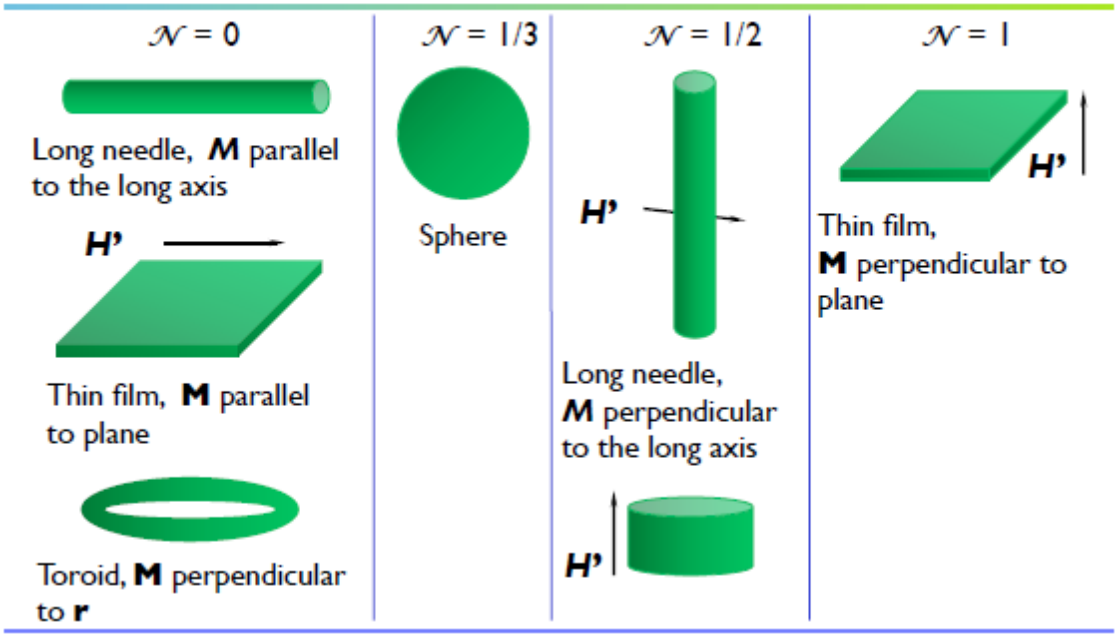

Figure 2.1 Demagnetizing Shape Factors.

Coey, J. M. D. (2010). "Magnetism and Magnetic Materials by J. M. D. Coey." Cambridge Core.

Scientific understanding of magnetism began in 1820, when Oersted discovered the connection between electricity and magnetism. By watching a current-carrying wire close

to a compass deflect the needle, Oersted realized electricity produced the same type of invisible field as magnets. Michael Faraday, during the same period, demonstrated and mathematically explained the principle of induction by creating a simple electric motor with a steel magnet, a current-carrying wire and a dish of mercury (Coey 2010). After looking through published work and performing electromagnetic experiments, James Clerk Maxwell formulated his four famous equations that relates electricity, magnetism and light.

$$1. \quad \nabla \cdot \mathbf{D} = \rho_V$$

$$2. \quad \nabla \cdot \mathbf{B} = 0$$

$$3. \quad \nabla \times \mathbf{E} = -\frac{\partial \mathbf{B}}{\partial t}$$

$$4. \quad \nabla \times \mathbf{H} = \frac{\partial \mathbf{D}}{\partial t} + \mathbf{J}$$

Figure 2.2 Maxwell's set of four equations that describe the world of electromagnetics.

Source: Bevelacqua, P. (2019). Maxwell's Equations. [online] Maxwells-equations.com.

In these set of equations, Maxwell relates electric and magnetic field (B and E) at a point in free space to the distribution of electric charge and current, p and J in a surrounding space. The solution to the equations represents the coupled electromagnetic wave with quantifiable wavelength (λ) and frequency (f) at the speed of light (c). Lorentz equation (Eq. 2), formulated around the same time, mathematically describes the magnetic force acting on a moving charged particle in a magnetic and electric field. Both of these

equations describe the interactions involving electromagnetic force, torque, energy, momentum, and angular momentum.

$$F = q(E + v \times B) \quad (2)$$

Technological and industrial advancements occurred more rapidly with the utilization of electrical and magnetic power. However, the few types of magnet available such as carbon steel, known to produced weak and deteriorating magnetic fields, was replaced by iron-cored electromagnets; popular choice for electric motors and generators. The main problem with electromagnets were required heavy and bulky electric coils to produce strong magnetic field. Research and development efforts concentrated on the origin of magnetism, which was not well understood until the emergence of quantum mechanics and relativity.

It turns out the current source or quantized electric currents that create the continuous magnetic field for solids was caused by the intrinsic spins and orbital motions of the electrons. The unit of magnetic quantity at a very small scale is called magnetic moment (m) and is expressed as:

$$m = IA \quad (3)$$

The symbol I represents current that flows, measured in amps, through the area A. Magnetic moment (A m^2), the elementary quantity in solid-state magnetism, is also the current density at a point. Electrons are the main source of magnetic moments in solids, due to its angular momentum. The orbital moment is an electron revolving around a nucleus of charge Ze in circular orbits under the influence of the Coulomb potential. The

electron also possess spin angular momentum with quantum number s = ½, which represent two possible orientations in a magnetic field, ‘up’ and ‘down’.(Coey 2010)

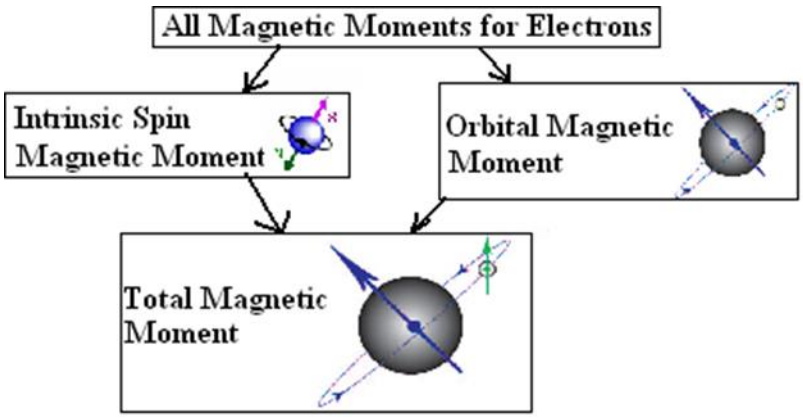

Figure 2.3 Electron possesses both an orbital magnetic moment and spin magnetic moment.

Source: Y. Kakehashi, Modern Theory of Magnetism in Metals and Alloys, Springer Series in Solid-State Sciences 175, DOI 10.1007/978-3-642-33401-6_1, Springer-Verlag Berlin Heidelberg 2012

The magnetization M of a body is the collection of tiny circulating electric current or elementary atomic magnetic moments and is defined by the ratio of the magnetic moment and volume of the solid (A/m). Magnetization is the intrinsic property of the material and magnetic moment is a property of a magnet as demonstrated in the figure below.

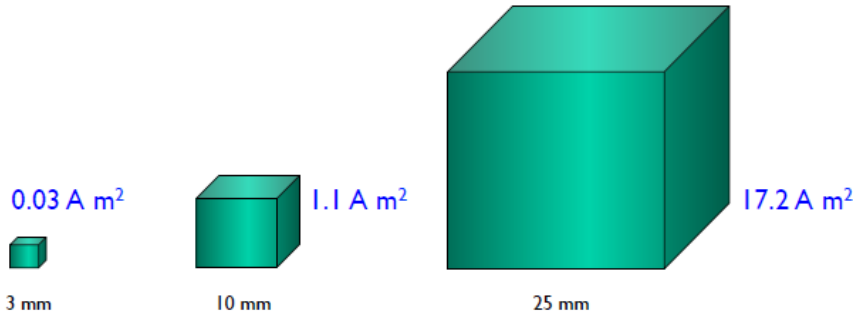

Figure 2.4 Demonstration of how magnetic moment is proportional to volume.

Source: Coey, J. M. D. (2010). "Magnetism and Magnetic Materials by J. M. D. Coey." Cambridge Core.

2.1.2 Coercivity and Hysteresis Loop Analysis

A new group of magnetic materials called hexagonal ferrites were the first artificial ferromagnetic materials and made the fabrication of magnets into different shapes and sizes possible. During the 1950s, scientists from the Philips Laboratories developed processes that manipulated the materials' microstructure to created "hard" magnetic materials that can withstand its own demagnetizing field. The hysteresis loop analysis was the analytic method of choice for understanding the irreversible nonlinear response of magnetization M to an applied magnetic field H.

Typical hard magnetic materials would have a broad M(H) hysteresis loop (Fig. 2.5) with a large residual magnetic flux M_s that exists at zero H field, known as the material's remanence (B_r) and a point on the hysteresis loop that defines the material's ability to resist demagnetization called coercivity (H_c). The second quadrant of the graph shows how magnet will behave under an applied magnetic field H_d. The broadness and squareness of this quadrant define the magnetic quality of a permanent magnet (Coey 2011).

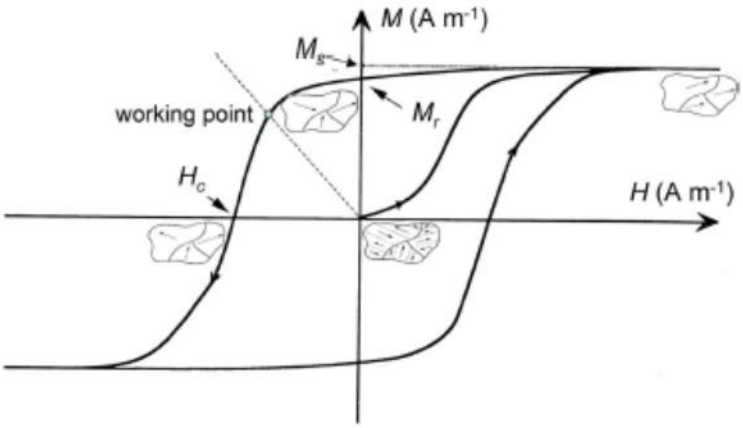

Figure 2.5 An M(H) hysteresis loop for a hard-magnetic material, with indications of the crystallite structure and domain structure at different points around. The dotted line, with slope-1/N intersects the loop in the second quadrant at the working point of the magnet.

Source: Coey, J. M. D. (2011). "Hard Magnetic Materials: A Perspective." Magnetics, IEEE Transactions on 47(12): 4671--4681.

Figure 2.6 illustrates a typical hysteresis loop of a soft magnet without the broadness or squareness at the second quadrant. The magnetic material becomes demagnetized as soon as it is under magnetic field. The main difference between hard and soft magnets is the presence impurities in magnetic composition. Hard magnetic materials contain impurities that prevent the misalignment of electron spins leaving behind its residual magnetization after the external magnetic field is removed. Soft magnetic materials do not possess impurities that can prevent misalignment of the atomic moments. They are temporary magnets, readily losing their magnetization as soon as the field is removed allowing easy switching from magnetized to demagnetized state. (Aoki, Orimoto et al. 2017)

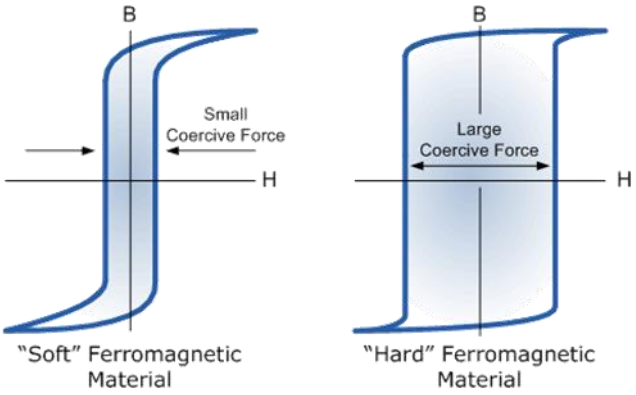

Figure 2.6 Hysteresis Loops of the Soft and Hard Ferromagnetic Materials

Source: Magnetic Hysteresis Loop including the B-H Curve. (2018, February 09). Retrieved from https://www.electronics-tutorials.ws/electromagnetism/magnetic-hysteresis.html

2.1.3 Magnetic ordering and Susceptibility

Another magnetic property, susceptibility, measures the degree of a material becoming magnetized under an applied magnetic field. It is represented as the dimensionless proportionality constant χ which is the ratio magnetization M to the applied magnetizing field intensity H (Blundell and Thouless 2003). The constant divides most materials (Fig. 2.7) up into two group: materials with value $\chi > 0$ demonstrate *paramagnetism*, while materials with value $\chi < 0$ demonstrates *diamagnetism*.

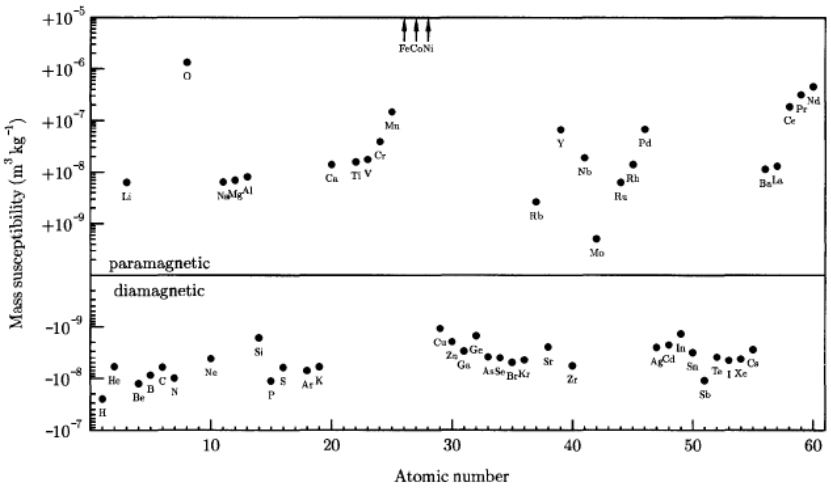

Figure 2.7 The mass susceptibility of the first 60 elements in the periodic table at RT, plotted as a function of the atomic number. Fe, Co, and Ni possess spontaneous magnetization with applied magnetic field.

Source: Blundell, Thouless 2003 "Magnetism in Condensed Matter", American Journal of Physics 71, 94 (2003); https://doi.org/10.1119/1.1522704

Materials that possess diamagnetism have a weak and negative magnetic susceptibility. A magnetic field applied to the material will be slightly opposed. They are typically ionic salts such as NaF, KCl, KBr and NaCl with unpaired electrons that have closed shell structures, like the noble gases Ne and Ar. Paramagnetic materials reveal positive susceptibility induce by the internal magnetization parallel to the applied field. When the magnetic field is applied, the degree of atomic moments aligning collectively depends on the strength of the applied magnetic field. The degree of alignment is temperature sensitive; the increase of temperature increases the randomization of the alignment. This inverse relationship between the temperature and magnetic susceptibility for paramagnetic materials is shown in the equation below:

$$\chi_m = C/T \tag{4}$$

C is known as the Curie constant define by the Curie's Law, which describes how the magnetization of paramagnetic material is directly proportional to the applied magnetic field. At a certain temperature, the spontaneous magnetization due to alignment of the atomic moments quickly falls to zero at the Curie temperature T_C. Above this critical temperature the material follows the Curie-Weiss law, shown below.

$$\chi_m = C/(T - T_C) \quad (5)$$

Antiferromagnetic materials possess coupling of electron spins with anti-parallel alignment against one another. The atomic sublattice moments are equal but aligned in opposite direction resulting in a zero-net magnetization. These materials have antiferromagnetic transition which occurs at the Neel temperature T_N. It is possible to switch an antiferromagnet into a ferromagnet if a very large field is applied. Transition-metal oxides and fluorides are frequently antiferromagnetic, as are Cr, Mn and many of their alloys (Coey 2010). *Ferrimagnets* have similar crystal structure and spin alignment as the antiferromagnets but the sublattice moments are unequal producing a spontaneous magnetization. Most oxides that possess a net ordered magnetic moment are ferrimagnetic. Magnetite, which have a spinel structure with formula Fe_3O_4, is a ferrimagnet.

Ferromagnetic materials are known to be self-saturating, or "spontaneously magnetized" materials because they possess permanent magnetic moments in the absence of an external magnetic field. Permanent magnetic moments arise from the uncancelled electron spins due to the electronic structure and coupling interactions of electron spins of adjacent atoms. Above Curie temperature T_c, ferromagnetic material becomes paramagnetic and its susceptibility follows Curie-Weiss law. Below its Curie temperature,

the intrinsic field generated becomes so strong that it can magnetize the substance to saturation even in the absence of an applied field.

Ferromagnetic materials are made up tiny domains or small-volume regions of magnetic moments aligned in the same directions. Adjacent domains are separated by domain boundaries with each domain spontaneously magnetized to a saturated value of M_s. The whole magnetic body possess a net magnetization of zero if the assembly of domains are not aligned. Application of a strong magnetic field converts the multi-domain structure into a single-domain system, all magnetized at the same direction. The direction of magnetization changes across the boundaries and the magnitude of magnetization in the material will be the vector sum of magnetization of all the domains as shown in the figure below.

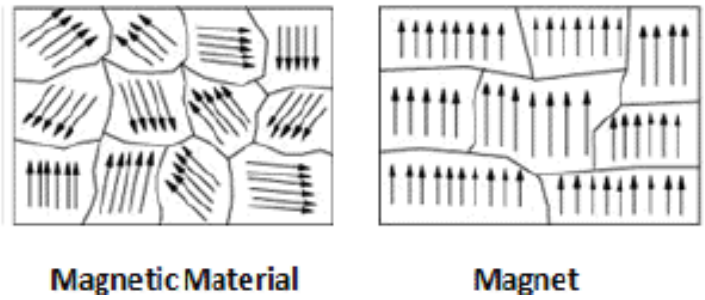

Figure 2.8 Domains not aligned to the left; Domains aligned due to magnetizing force

Source: Garrett, Casey."Caseygarrettphysics". Caseygarrettphysics.Blogspot.Com, 2018, http://caseygarrettphysics.blogspot.com.

Important property of permanent magnetic materials is the ability to produce stray field or the H field created by its own volume. This is different from the demagnetizing field is the H-field created within its volume. The air gap, as shown in Fig. 2.9, is the surrounding volume outside of the magnet and the energy density stored can be defined

by its maximum energy product $|BH|_{max}$ (unit: kJ/m^3 or MGOe). The $|BH|_{max}$ represents the area of the largest rectangle that can be inserted in the second quadrant of the B-H loop below which defines the quality of the ferromagnetic materials. It can enhanced by modifying structure-sensitive magnetic properties such as the residual magnetic flux (B_r) and the coercivity, (H_c), and/or by enhancement of fundamental intrinsic properties such as the saturation magnetization, (M_s) (Jimenez-Villacorta and Lewis 2014). The load line and the working point (the intercept of the extrinsic demagnetizing curve) represents the operating point of the magnet at maximum efficiency.

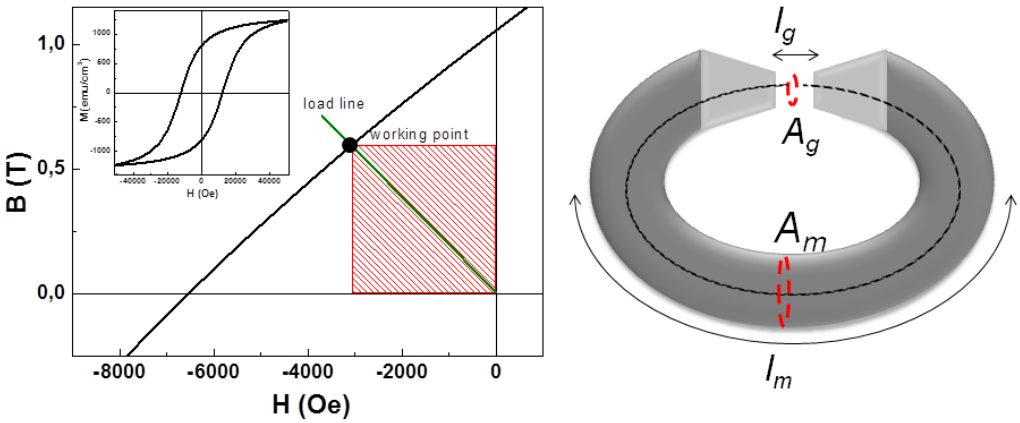

Figure 2.9 a) Plot of the 2nd quadrant of the B-H hysteresis loop. The shaded area represents the maximum energy product, $(BH)_{max}$ b) Depiction of the open magnetic circuit comprised of a permanent ring magnet, two soft magnetic ends to guide the magnetic flux and an empty airgap

Source: Jimenez-Villacorta, F. and L. H. Lewis (2014). "“Advanced Permanent Magnetic Materials”." ResearchGate: 30.

2.1.4. Origins of Ferromagnetism

The origin of magnetism at the atomic levels arise from the electron motion around the nucleus and the spins on the electrons. Long range magnetic ordering occurs when unpaired electrons align parallel to each together in the domain which disappears about the critical temperature known as the Curie point (Coey 2010). Ferromagnetism and the Curie temperature was explained by Weiss's molecular field theory where he postulated an internal 'molecular field' with the Weiss coefficient n_w is proportional to the magnetization for ferromagnetic materials as show below:

$$H^i = n_w M \tag{6}$$

H^i has to be large for the material to maintain spontaneous magnetization at room temperature.

Exchange interaction is the foundation of the effective field H^i which reflects on the Coulomb repulsion of two nearby electrons and the Pauli principle which forbids the two electrons to enter the same quantum state. There is an energy difference between the two different configurations of the spins of neighboring atoms. Electrons are indistinguishable fermions, so the only solution to this total wave function of the two electrons is going to be antisymmetric. When a bond forms of two atoms form, there are two molecular orbits, a spatially symmetric bonding orbital φ_s , with electronic charge piled up between the atoms, and a spatially antisymmetric antibonding orbital φ_a having a nodal plane with no charge midway between them (Coey 2010). These symmetric and antisymmetric spin functions are known as the spin triplet and spin singlet states. Two electrons in a spin triplet state with parallel spins avoid each other while electrons are in the spin singlet state, with antiparallel spins, can be found in the same place. The energy

splitting between the singlet state and the triplet state (Fig. 2.10) is twice the exchange integral *J*.

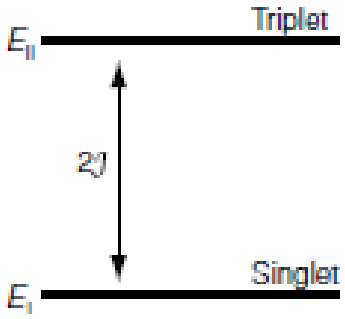

Figure 2.10 Example of the splitting between the spin singlet and spin triplet states for the H_2 molecule.

Source: Coey, J. M. D. (2010). "Magnetism and Magnetic Materials by J. M. D. Coey." Cambridge Core.

Heisenberg generalized the many-electron atomic spins S_1 and S_2, in his famous Hamiltonian equation:

$$H = -2JS_i \cdot S_j \quad (7)$$

S_i and S_j are dimensionless spin operators and the units of the exchange constant *J* is energy (Joules). $J > 0$ means a ferromagnetic interaction or the tendency for the two spins to align parallel to each other and $J < 0$ indicates an antiferromagnetic interaction or the tendency for the two spins align antiparallel. The Heisenberg Hamiltonian tell us if the exchange interactions result in the coupling of the atomic spins.

Atoms with orbitals have individual electrons have spin and orbital angular momenta that are coupled in isolation resulting in orbital quantum numbers S and L. When spin-orbit interaction occurs the coupling of L and S together to form different J-states of a term are known as multiplets (Fig. 2.11). The ground state multiplets are the only ones that occupied at room temperature and determines the magnetic properties of the atom.

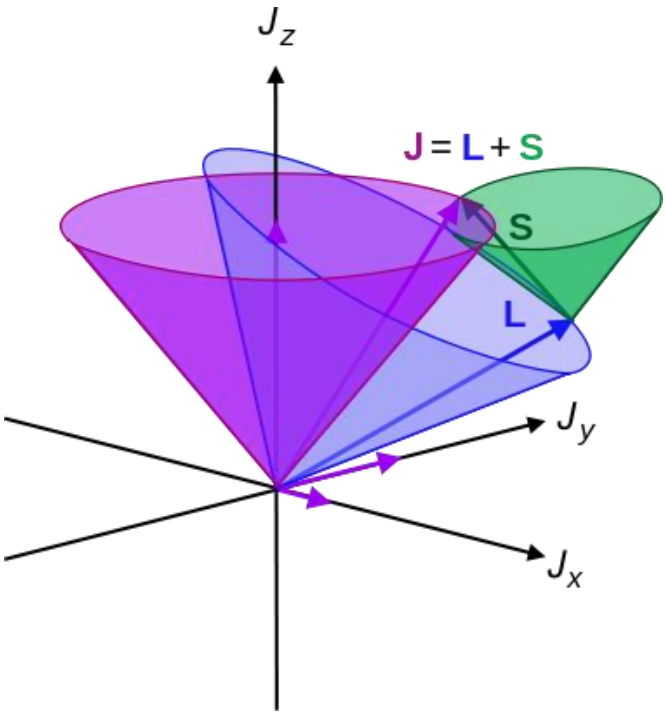

Figure 2.11 Illustration of L-S coupling. Total angular momentum J is purple, orbital L is blue, and spin S is green.

Source: "10.4: Atomic Term Symbols and Wavefunctions." Chemistry LibreTexts, National Science Foundation, 26 Nov. 2018, chem.libretexts.org/Bookshelves/Physical_and_Theoretical_Chemistry_Textbook_Maps/Book:Quantum_Mechanics__in_Chemistry_(Simons_and_Nichols)/10:_Angular_Momentum_and_Group_Symmetries_of_Electronic_Wavefunctions/10.4:_Atomic_Term_Symbols_and_Wavefunction

Magnetic anisotropy is the tendency of the ferromagnetic domain to align among one or more easy axes. *Anisotropy energy* E_a is the energy term that describe the tendency for magnetization to lie along an easy axis:

$$E_a = K_1 \sin^2\theta \tag{8}$$

The three factors that defines magnetic anisotropy describes the sample shape, compositional crystal structure and texture at microscale. Shape anisotropy is related to the sample demagnetizing field H_d and describe how magnet can be fabricated in any shape without demagnetizing itself. Magnetocrystalline anisotropy is an intrinsic property that reflects on the crystal symmetry or how different directions of the microstructure behaves

towards an applied field. There is a small dipolar 'two-ion' contribution of magnetostatic origin, but the main source is the 'single ion', electrostatic crystal field interaction acting in conjunction with spin-orbit coupling. This leads to the requirement that the crystal structure itself has to be uniaxial. (Skomski and Coey 2016). Induced anisotropy is the creation of the easy direction of magnetization by some form of physical mechanism or creating atomic scale texture.

2.1.5 Organic Ferromagnetism

Organic magnetic materials are relatively new but expected to have a huge impact because they have plastic properties, lightweight, low density, made from abundant source, and possess tunable magnetic properties that can be coupled with other properties. The slow progress and development of these materials is due to the stabilization of the radical electrons within the organic system. Radical electrons are highly reactive and can easily form chemical bonds in thermal and chemical environment. The recent surge with organic based magnets has demonstrated magnetic ordering temperature exceeding room temperature and unusual magnetic properties ranging from ferromagnetism to antiferromagnetism.

Typical inorganic, atom-based magnets contain unpaired d- or f-type electrons that contributes to magnetism. The magnetism in organic materials reside in the p-orbitals through the intramolecular exchange interaction from the alignment of the π system. These high-spin (total spin quantum number $S \geq 1$) organic molecules perform spin alignment differently from the spin pairing of typical covalent bonding of organic molecules which possess singlet ground states ($S = 0$) separated from the nearest excited triplet states ($S = 1$) by tens of kcal mol^{-1}. To design and synthesize these high-spin organic molecules

requires the inversion of the large energetic spin pairing to provide high-spin ground state (Gallagher, Olankitwanit et al. 2015). Also, the magnetic coupling energy must surpass the thermal energy that randomize the electron spins, creating magnetic ordering with spins that are aligned (ferromagnetic) or opposes to each other (antiferromagnetic).

Organic monoradicals are the most basic organic spin-bearing units (S = 1/2), carrying one unpaired electron. The ultimate goal in the molecular design of high-spin organic molecules is producing conjugated, multiple radical units or spin centers (Gallagher, Olankitwanit et al. 2015). The spins coupling of two radicals forms a diradical in a high-spin ($S \geq 1$) ground state. This interaction creates this large separation between high and low excited spins states, called a singlet triplet energy gap (ΔE_{ST}), which can be determined by calculating the exchange coupling constant (J), using the simplified Heisenberg–Hamiltonian for two electrons:

$$H = -2JS_1 \cdot S_2 \tag{9}$$

The first step of producing high-spin ground states of hydrocarbons is understanding Kekulé and non-Kekulé molecules. Kekulé structures, such as benzene, are alternating double and single carbon–carbon bonds representation of organic molecules. There are two possible bonding arrangements (two alternation patterns) or two Kekulé forms of the same molecule which is known as resonance. Kekulé-type conjugated molecules are shown in the left-hand side of Fig. 2.12. On the right side are non-Kekulé-type conjugated molecules whose structure contains ≥ 2 atoms that are not π bonded and have two or more formal radical centers.

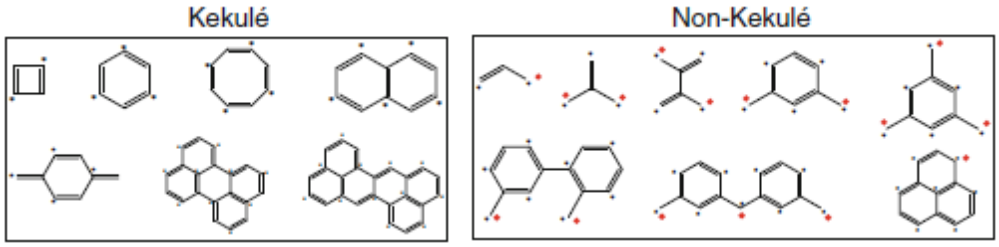

Figure 2.12 Kekulé and non-Kekulé forms of conjugated molecules.

Source: Aoki, Y., Y. Orimoto and A. Imamura (2017). Quantum Chemical Approach for Organic Ferromagnetic Material Design | SpringerLink, Springer, Cham.

One example of the diradical formation is the combination of the methyl radicals as the spin centers with ethylene as the coupling unit to form two different molecular structure, trimethylenemethane (TMM) and 1,3 butadiene. The non-Kekulé molecule TMM possesses a triplet (S = 1) ground state with $\Delta E_{ST} \approx 16$ kcal mol^{-1} while the Kekulé molecule 1,3-butadiene possesses a singlet (S = 0) ground state with a very large energy gap ($\Delta E_{ST} \approx -74$ kcal mol^{-1}) which judging on how wide the energy gap is expected to be a closed-shell molecule(Aoki, Orimoto et al. 2017).

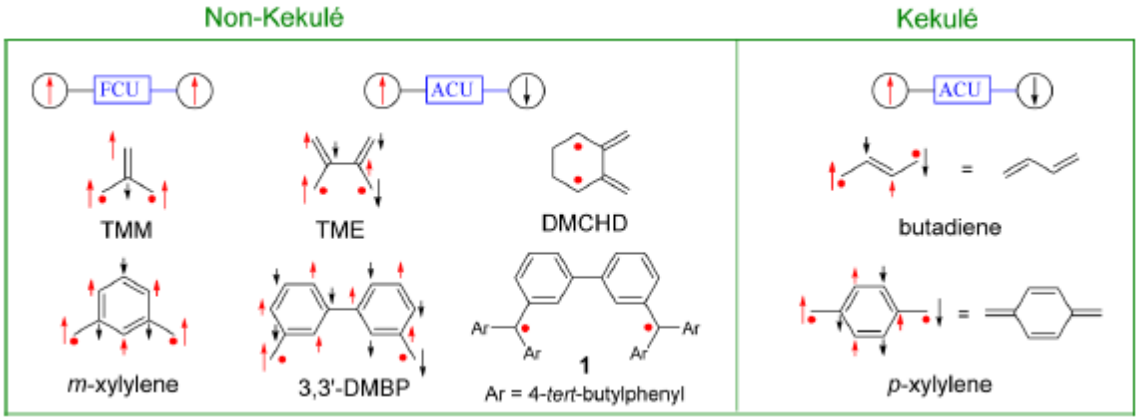

Figure 2.13 Ferromagnetic and antiferromagnetic coupling predicted using parity models.

Source: Aoki, Y., Y. Orimoto and A. Imamura (2017). Quantum Chemical Approach for Organic Ferromagnetic Material Design | SpringerLink, Springer, Cham.

The next step in producing high spin states organic molecule from non-Kekulé molecules is understanding "disjoint" and "non-disjoint" molecules. In organic chemistry, the frontier molecular orbitals of a compounds are referred to the "frontier" of electron occupation or the region where chemical reaction or redistribution of electrons occurs. At this level, highest-energy occupied molecular orbitals (HOMO) is involved in electron donation, while the lowest-energy unoccupied molecular orbitals (LUMO) accept those electrons. When neighboring frontier MOs are approximately equal in energy, this can lead to two singly occupied MOs (SOMOs). According to researchers Borden and Davidson, the two SOMOs can be classified as either disjoint (not spatially coinciding at any atoms) or non-disjoint (spatially coinciding at some atoms)(Borden, Davidson et al. 1978) as explain in the diagram down below. Disjoint SOMOs have very weak exchange coupling with small $|\Delta E_{ST}|$ while non-disjoint SOMOs possess strong and ferromagnetic exchange coupling. The non-disjoint SOMOs have electron spins that are aligned, reducing their Coulombic repulsion within the spatial region.

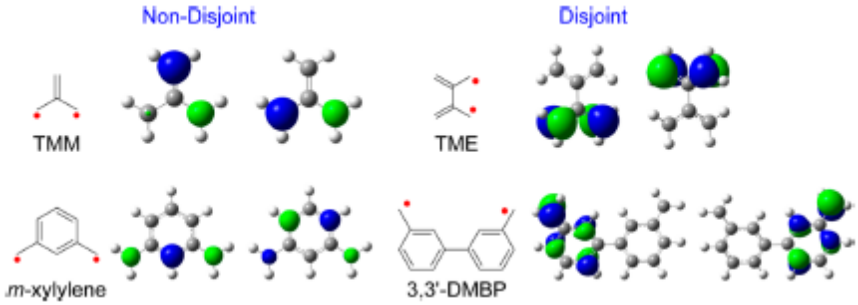

Figure 2.14 Singly occupied MOs (SOMOs) of triplet states for disjoint and non-disjoint non-Kekulé diradicals.

Source: Borden, W. T., E. R. Davidson and P. Hart (1978). "The potential surfaces for the lowest singlet and triplet states of cyclobutadiene." J. Am. Chem. Soc. 100(2): 388--392.

Understanding the exchange interactions between radical electrons is one of the essential parts of building an organic ferromagnetism system. Two main types of strategies for the designing complex ferromagnetic systems when considering the exchange interactions. The first one aims at the development of radical crystals using TS intermolecular interactions, and the second strategy focuses on the preparation of radical polymers using intramolecular interactions.

Radical crystals usually designed by stacking small radical molecules and are the dominant contributors to the ferromagnetic properties of the whole system. Many magnetic systems based on the stacked molecule approach have been investigated from both theoretical and experimental studies with various organic molecule-based radical crystals including nitronyl nitroxide (NN)-based crystals and charge-transfer salt crystals. The design of radical polymers by arranging as many radical spins as possible in a system of intramolecular TB exchange interactions such as π-conjugation is the essential feature. In general, TB-type exchange interactions are stronger than TS-type interactions. Thus, radical polymers are expected to have TC values much higher than those of radical crystals. In practice, polymers with very high spin multiplicities reported by Rajca et al. In addition, a hybrid strategy that fits between the TS and TB approaches has also been proposed

Another set of carbon system that have demonstrates ferromagnetism are graphitic materials, which is closely related to the lattice imperfections induced by proton-irradiated graphite spot or specially prepared pyrolytic graphite containing a high defect concentration. They have also been observed with polymerized fullerenes, carbon nanofoam, proton irradiated thin carbon films, and nitrogen and carbon ion implanted nanodiamond (Červenka, Katsnelson et al. 2009). There have been many theories about the

origin of ferromagnetism. Some have suggested the is mixture of carbon atoms with alternating sp^2 and sp^3 bonds, presence of a negatively curved graphitic surface containing seven- or eight-membered rings, and the existence of zigzag edges. Recently, the application of spin-polarized density functional theory (DFT) calculations have concluded that point defects in graphite such as vacancies and hydrogen-terminated vacancies are magnetic in disordered system with preserved stacking order of graphene layers.

2.1.6 Additive Manufacturing

Additive manufacturing (AM) in the past 25 years has made an impact due to it processing flexibilities with materials such as plastic, metal, ceramic and concrete. It is highly customizable process with the ability to fabricate solid parts with geometric and multi-material complexities. The ASTM F42 Technical Committee defines additive manufacturing (AM) as the "process of joining materials to make objects from 3D model data, usually layer upon layer, as oppose to subtractive manufacturing methodologies" (Guo and Leu 2013). Some of the AM processes include stereolithography (SLA), fused deposition modeling (FDM), selective laser sintering (SLS), laminated objective manufacturing (LOM) and laser metal deposition. It has caught the manufacturing interests because it near net shape capability within the production process. It provides way to the eliminate or reduce finishing steps, create semi-finished products that are as close as possible to the desired final geometry and technological characteristics and minimizing the raw material usage (Marini, Cunningham et al. 2017). It has made tremendous progress in specialized industries such as R&D, aerospace, biomedical and automotive because of its benefits conventional subtractive manufacturing cannot provide.

Thermoplastic polymer materials such as acrylonitrile butadiene styrene (ABS), polylactic acid (PLA), polyamide (PA) and polycarbonate (PC) as well as thermosetting polymer materials like epoxy resins are popular choices in the AM field. However, most 3D printing of polymer products are used mainly as a conceptual tool rather than functional components, because the final 3D print lack the strength and functionality. The need to create new industrial and commercial applications with 3D printed polymers has been the catalyst for the recent development of 3D printing of polymer composites. 3D printing of polymer composites could solve these problems by combining the matrix and reinforcements to achieve a more useful structural or functional properties non-attainable by any of the constituent alone (Wang, Jiang et al. 2017). Inserting particle or fiber reinforcements into polymers has been well known to enhance properties of polymer matrix composites. Add the element of creating components with complex geometry without the wasteful material removal process will create 3D printed composites with process flexibility and high performance.

Down below are a list of some of the many AM processes that are well established and brings a unique fabrication perspective. Some apply thermal energy from laser or electron beam onto metal or plastic powders while others use inkjet or extrusion printhead to accurately deposit material on layer-by-layer process.

Stereolithography (SLA) is one of the earliest and most common 3D printing process that uses UV light to cure photopolymer resin. The UV light goes through a controlled path as it radiates its beam onto a thin layer photocurable resin inside a reservoir. When the resin is polymerized at specific points, the platform lowers laying on top another

thin layer of uncured polymer ready to be printed in a patterned fashion. Acrylic and epoxy resins are the commonly used printing material for this AM process.

Using the SLA process requires the understanding of the curing reactions during polymerization to control the final quality of the printed parts. The prints can be altered or modified with photoinitiators and UV absorbers additives. Other important parameters used in this technique includes the intensity of laser power, scan speed and duration of exposure affect the curing time and printing resolution. SLA are well known for their high printing resolution and is a nozzle free technique that gets rid of the common problems in 3D printing of nozzle clogging(Wang, Jiang et al. 2017).

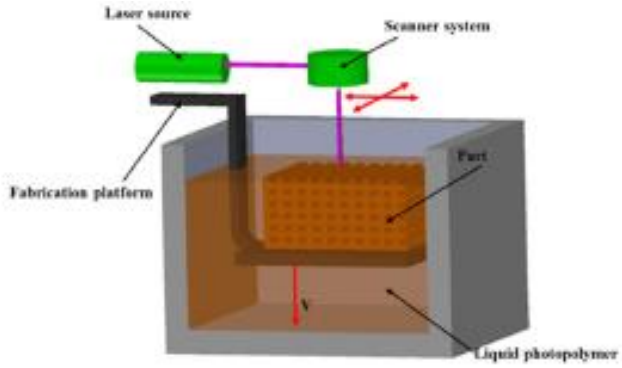

Figure 2.15 SLA setup with the laser source, scanner system and bed platform.

Source: Wang, X., M. Jiang, Z. Zhou, J. Gou and D. Hui (2017). "3D printing of polymer matrix composites: A review and prospective." Composites Part B 110: 442--458.

Selective laser sintering (SLS) is an AM process that generates complex 3D parts by applying a focused laser beam onto the deposited successive layers of powder material. The SLS printer can precisely deflect laser beams with galvano mirrors onto a successive powder layers with great print resolution (thickness: 20-150 μm). The laser beam sinters the powder causing them to fuse together through molecular diffusion mechanism. Prints are typically fabricated in argon or N_2 environment using a laser system such as CO_2 laser,

lamp or diode pumped Nd:YAG laser, disk or fiber laser (Rombouts, Kruth et al. 2005). There are different types of binding mechanism with defines the different techniques with SLS. *Solid State Sintering* conducts the thermal process between $T_{melt}/2$ and close to the material's melting temperature. Diffusion process occurs when the neck formation occurs in between adjacent powder particles (see Fig. 2.16). *Liquid Phase Sintering* (LPS) technique involves the combination of the solid powder particle and liquid binder material.

To fabricate a fully dense object and avoid lengthy processing cycles, the *Selective Laser Melting* (SLM) was developed. Both polymer and metallic powders can be used in this technique. SLM uses a laser to melt successive layers of powder. The laser will heat particles in specified places on a bed of powder until completely melted. The machine will then successively add another bed of powder above the printed layer and repeat the process until the object is completely finished. For metal AM processing parameters such as laser absorption, surface tension and viscosity of the liquid must be considered

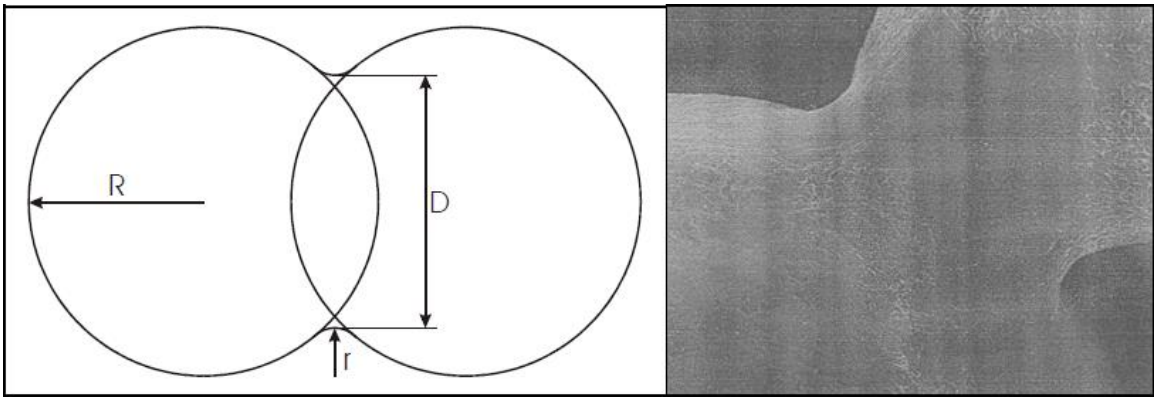

Figure 2.16 On the left side, neck formation in Solid State Sintering and on the right sided neck formation between two stainless steel powder particles.

Source: Kruth, J.-P., P. Mercelis, J. Van Vaerenbergh, L. Froyen and M. Rombouts (2013). "Binding mechanisms in selective laser sintering and selective laser melting." Rapid Prototyping Journal.

Direct Ink writing is a three-dimensional process that fabricate periodic structures comprising of colloidal, polymeric, composites or semiconductor materials, critical in many technological applications that includes sensors, microfluidics, photonics, and tissue engineering. The term “direct ink writing” describes fabrication methods that employ a computer-controlled translation stage, which moves a pattern-generating device, that is, an ink-deposition nozzle, to create materials with controlled architecture and composition (Lewis 2006).

The ink designs applied to this technique include highly shear thinning colloidal suspensions, colloidal gels, polymer melts, dilute colloidal fluids, waxes, and concentrated polyelectrolyte complexes. The solidification process are liquid evaporation, gelation, or a temperature- or solvent-induced phase change. Because of the variations of the ink composition there must be special consideration with the printing parameters, rheological properties, high aspect ratio and spanning feature. The big advantage for direct ink writing technique is the fabrication of 3D architectures at the micro- and sub-microscale levels.

Fused deposition modeling (FDM) common printing process the involves the extrusion of filament from movable printer head and out through a nozzle around the melting temperature. The liquid thermoplastic material is set down in a linear fashion, layer by layer onto the build platform fusing with previous layer and solidify immediately. The popular choice of thermoplastic materials includes polylactic acid (PLA), acrylonitrile butadiene styrene (ABS), polycarbonate (PC), polyamide (PA) with new materials gaining ground like ULTEM, polycarbonate, Polyphenylsulfone (PPSF), and fiber/metal/ ceramic polymer composites. FDM provides a large selection of materials with great print accuracy, easy operation, low maintenance and equipment costs. Some of its disadvantages

include the requirement of supports, build time, seam line between layers and delamination caused by temperature fluctuation. The figure below shows the basic FDM structure from the filament spool to the printing of the object.

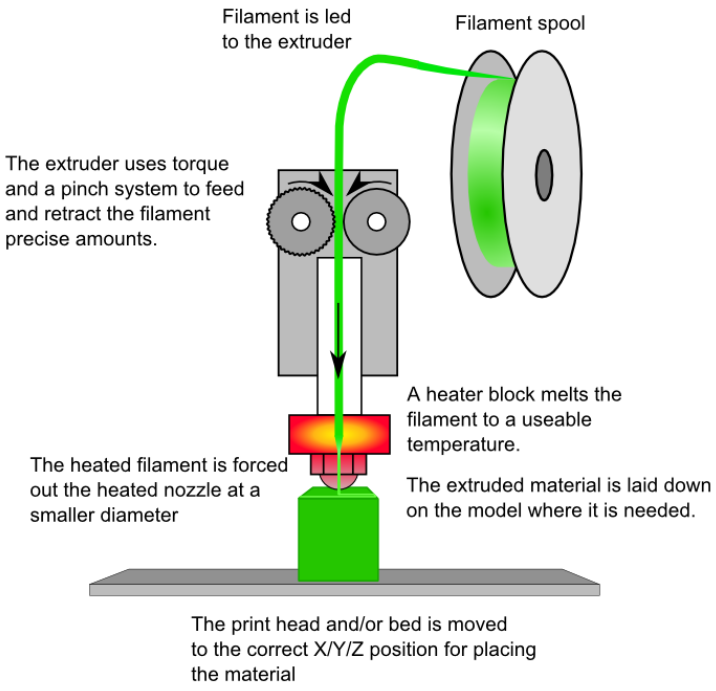

Figure 2.17 Basic FDM Setup.

Source: Wang, X., M. Jiang, Z. Zhou, J. Gou and D. Hui (2017). "3D printing of polymer matrix composites: A review and prospective." Composites Part B 110: 442--458.

There are various filament feed mechanisms responsible for delivering and applying force to polymeric filament so it can guide it smoothly into the liquefier (heater) and nozzle. The liquefier heats and melt the polymer before it reaches the nozzle. This is achieved by conduction via contact between the moving filament and a metal conduit whose temperature is maintained using a resistively heated coil embedded in a metal block. The temperature sensor is placed in close proximity to the nozzle for temperature control.

The 3D printer's motion system positions the print-head and platform in the 3D space. The motion system comprises three linear actuators that are responsible for a Cartesian direction vector (X, Y, Z). The rotary motion of the DC motors responsible for the X/Y motion of the print-head converts the linear motion by a belt drive or lead screw and connecting the two such orthogonal axes in series. Z motion of the bed platform is performed using a linear actuator (stepper motors) oriented vertically (Wang, Jiang et al. 2017).

2.2 Literature Review

2.2.1 Introduction

Recently, conventional manufacturing methods are lagging in the area of product development due to the slow testing and long validation procedures. Miniaturization and the mass customization of products are in high demand, forcing different sectors of manufacturing to redesign and develop new innovative manufacturing processes. This is especially true in the development of products that use magnetic materials, where the fabrication processes of custom magnet shapes such as sintering, hot-pressing, or injection molding are energy-, time-and cost-intensive and requires special tooling. Conventional manufacturing techniques restrict and prolong the design of new and complex structures. Applying new form of rapid manufacturing methods, such as AM, for magnetic materials during prototyping and end-product phases will be very beneficial.

Applying AM methods to magnetic materials will open up the necessary design of freedom and place existing magnetic materials into new applications such as sensors. 3D printers, computer simulation and topology optimization techniques are together enhancing the fabrication process of magnetic materials opens up new possibilities which would be

inconceivable with other techniques. Organic based magnets are a new emerging class that bring a unique material properties and will further the development in magnet fabrication.

2.2.2 3D Printing of Magnetic Bonded Composite

AM methods have recently been applied to permanent magnets to create final products with unique shapes and interest magnetic properties. For example, 3D metal printing technology based on laser engineered net shaping (LEN) was utilized by authors Geng and Nlebedim to produce bulk specimens made of different Fe-Co composition. AM technology developed for fabricating metal parts directly from a computer-aided design (CAD) solid model by using metal powders injected into a molten pool created by a focused, high-powered laser beam. (Geng, 2016) There are much more challenges to consider when applying metal printing to RE-Fe-B magnets due to their high melting temperature, different evaporation rates of each elements and the complexity in the ternary phase diagram. Very recently, extrusion printing of NdFeB bonded magnets have been explored and being successful

Research group headed by Dieter Suess in Vienna' TU Wien demonstrated a way to fabricate polymeric bonded magnet with a complex shape using a Fused Deposition Modeling (FDM) printer. They created a collection of research revealing that by utilizing the capability of AM, it was now possible to print bonded magnet of complex shapes with locally tailored magnetic properties. In the paper "3D Print of Polymer Bonded Rare-Earth Magnets and 3D Magnetic Field Scanning with an End-User" a calibration method was used to setup a 3D scanning magnetic measurement system to measure the printed magnetic properties and compare it to finite element simulations solving the macroscopic Maxwell equations. The filament used in this experiment contained 45-65% NdFeB granules within

a polyamide matrix. The stray field of the printed permanent magnet was measured by 3D magnetic flux density measurement system install onto the 3D printer. This sensor was calibrated using calculated magnetic flux density of B of a predefined object and a reference field created by finite element simulation to formulate an optimization problem that was used to determine the calibration parameter of the sensor.

In the paper "Topology Optimized and 3D Printer Polymer Bonded Permanent Magnet for Predefined External Field" a topological optimization method was used to designed 3D printed bonded magnet with specific stray field characteristics. Density method used assumed the magnet consist of a solid isotropic microstructure made of elements with density that represent either 0 (void) or 1 (bulk) in the design domain Ωm. With this optimization method the group demonstrate the possibility of designing and building a magnet with the ability to maximize the external magnetic field at a small target. They validate the method with a volume constraint procedure, reverse engineering of a magnetic topology and constructing a ferromagnetic system with unknown geometry directly from field measurements.

With increasing innovation and miniaturization of electronics and its components, there is equally an increasing demand for an extremely efficient assembly system. Dr. Ravindra's Group in the research paper "Magnetic Field Assisted Heterogeneous Device Assembly" took on self-assembly technique by the magnetic field assistance of a group of small cylindrical solenoids. Deterministic approaches have used applied to deal with the statistics of the magnetic device's positions and movements, while dealing with the interacting forces in a controlled environment.

In order to make the small device assembly deterministic, the motion of the devices must be made predictable with high accuracy when adding some limits. In the experiment setup, there is a collection of solenoids used to generate a magnetic field that guides magnetic components through a predetermined path to its final destination. Simple sensing techniques were installed to detect any misfit and misalignments. Various solenoids with different geometric shapes were analyzed to provide a specific radial field strength for a particular current to overcome frictional forces.

Understanding the physics how a magnetic object move through magnetic field was the first step of designing the magnetic field assisted assembly system. Each current carrying solenoid generate a magnetic field B that can be calculated by Biot-Savart law:

$$B = \int \mu_0 I dl \times r/r^3 \tag{10}$$

The field is due to a cylindrical shape of the coil with length 2b and n turns has a field distribution given that can be broken down into B_ρ (radial) and B_z (transverse) magnetic field components(Kasisomayajula, Booty et al. 2012).

When an object with a magnetic dipole is place in the magnetic field created by the solenoid, there is an interaction, torque (τ), that is acting on the magnet due to the transverse component of the filed. The force on the magnetic object across the surface due to field gradient is given by the equation:

$$F = \nabla(\mu \cdot B) \tag{11}$$

To optimize the path of magnetic device, the geometric shape of the solenoid must be design for optimal field distribution. This is where AM process can be applied to develop ferromagnetic magnets with unique shape to achieve optimal field distribution with the assistance of topological methods.

It is important to understand the effect of binder on the magnetic properties of polymer bonded magnets. Mousavian et al. discuss how the selection of binders such as polypropylene, nylon 66, high impact polystyrene, polycarbonate and acrylonitrile butadiene styrene affects the magnetic properties Fe_3O_4 nanoparticles. Grujić et al. discuss about NdFeB powder in the bonded magnet determines the mechanical, viscoelastic and magnetic properties of composites have been observed using Scanning Electron Microscope (SEM), Dynamic Mechanical Analysis (DMA) and Super Quantum Interference Device (SQUID) magnetometer.

2.2.3 Development of Organic Based Magnets

Mahmood et al. performed self-polymerization of the tetracyanoquinodimethane (TCNQ) monomer (Fig. 2.19) in trifluoromethanesulfonic acid at 155°C to create an organic π-conjugated network structure. Within the polymer matrix contains highly stable spins along the π-conjugated polymeric chains. This is a significant feat for a purely organic material to achieve ferromagnetism without metal contamination. Computational analysis was applied for theoretical proof of the stable radical formation.

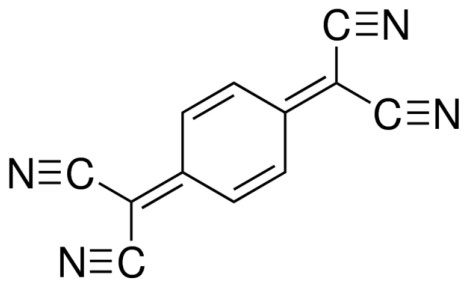

Figure 2.18 7,7,8,8-Tetracyanoquinodimethane monomer

Source: https://www.sigmaaldrich.com/catalog/product/aldrich/157635?lang=en&region=US

2.2.4 3D Printing of Organic Based Magnetic Materials

Huang's research group from Hong Kong Polytechnic University applied 3D printing method to construct a 2.5D multilayer cobalt-based organic ferromagnetic materials.(Huang, Yung et al. 2017) This is different extrusion process from FDM because there temperature setting requirement and the feedstock is colloidal liquid-based. They solves the material agglomeration, typical issue with inkjet printing, by combining the synthesized cobalt-based molecular materials with low volatility organic solvent to produce metal-organic ink. Droplet jetting technique was used with print speed (500 mm/min), printing period (9650 μs) and delay (704 μs). This is well-controlled viscoelastic response, so they flow through the deposition nozzle and then "set" immediately to facilitate shape retention of the deposited features even as they span gaps in the underlying layer(s).(Lewis 2006)

Some of the scientific efforts moving away from atom-based magnets and over to "plastic" magnet have fueled decades of research in creating purely organic magnets based on free radicals. From crystalline solid of small molecule radicals or charge transfer salts to radicals along a π conjugated backbone, it is still unclear if there are any organic materials out there with reproducible magnetic characteristics. Mahmood et al. recently reported on a purely organic material with ferromagnetic properties.

CHAPTER 3

MATERIAL CANDIDATES AND METHODS

3.1 NdFeB Bonded Composite

The rare earth (RE)-Fe-B Bonded composite used in this experiment for the FDM printing method was NdFeB bonded composite which consist of melt-spun RE-Fe-B powder and polyamide (PA12) binder. The next few sections will discuss about the NdFeB powder and binder materials in detail before going into the composite used for the AM experiment.

Figure 3.1 NdFeB Bonded Composites Granules used for the experiment.

3.1.1 RE-Fe-B

During the 1970's, R-T compounds (R = rare earth and T = 3d transition metal), SmCo and Sm_2Co_{17}, displayed the highest magnetic performance of any hard-magnetic materials due to its large magnetocrystalline anisotropy. These materials possessed a strong 3d-3d exchange interactions that stabilized the magnetic ordering against thermal agitation at high temperatures, which was perfect for high temperature applications such as automotive. Another discovery, the 3d-4f magnetic interactions, sustain the R- sublattice magnetization, allowing the 4f anisotropy stabilize above room temperature (Sagawa,

1987). The R-T compound with Sm can only exist with Co which are not as abundance as the rare earth elements Nd and Pr, pushing research efforts over to R-Fe binary compounds because of the abundance supply of Fe and its high magnetic moment. Years of research on the R-Fe binary compounds was unsuccessful but there was growing interests in the R-Fe-X ternary system. Sagawa et al. explored various elements X to create a new compound, $R_2Fe_{14}B$, with amazing magnetic properties comparable to the previous R-T compounds.

In 1984, Sumitomo Special Materials (SSMs) in Japan and General Motors (GM) in USA developed the compound $Nd_2Fe_{14}B$, using two different manufacturing methods in the production of the alloy, sintered and rapidly quenched. SSMs produced an anisotropic microcrystalline sintered magnet that resulted in a coarser microstructure which made them less reliant on the less abundant heavy rare-earth elements for magnetic performance at elevated temperatures. GM went with the rapidly quenching Nd–Fe–B for nanocrystalline net-shaped magnets that developed fine nanostructures to maintain coercivity. SSM's alloy of Nd_{15} $Fe_{77}B_8$ had an energy product of about 290 kJ/m^3, while GM produced isotropic permanent magnets with BH_{max} of about 114 kJ/m^3. They also had different business model with SSM handing out license to magnet manufacturers while GM produces and sold NdFeB powders to buyers that were willing to fabricate it as polymer bonded or hot-formed magnets.

The $RE_2Fe_{14}B$ crystals produces as sintered or rapidly quenched magnets are the same but the key difference between the two are their microstructures, specifically the grain size and grain boundary which controls the overall magnetic performance. Rapidly quenched process produces finer grain sizes which enhance the magnet's ability to resist

demagnetization and give higher coercivity advantage. Sintered magnets are developed for better grain orientation alignment which enhances the material's magnet flux density, B_r.

The compound composed of Nd, Fe, and about 1% of B with a tetragonal structure with lattice constants a = 0.880 nm and c = 1.221 nm. Tetragonal cell uniaxial magnetocrystalline anisotropy of the rare earth permanent magnet compound such as Neodymium is due to the electrostatic energy of localized 4f spin orbit-lattice interactions (Satoshi Hirosawa 2017). The atomic arrangement around Nd ion also affects its electrostatic interface. (Fig. 3.2) demonstrates the layered section of atomic arrangements in the $Nd_2Fe_{14}B$ crystal structure, how the pancake-shaped 4f orbitals of an Nd ion sits in an aspherical distribution of valence electrons which has larger density along the principal axis of symmetry of the Nd2Fe14B lattice (b), and a possible interface interaction with oxygen in which the Nd valence electrons moved toward the oxygen atom for bonding (c) (Satoshi Hirosawa 2017).

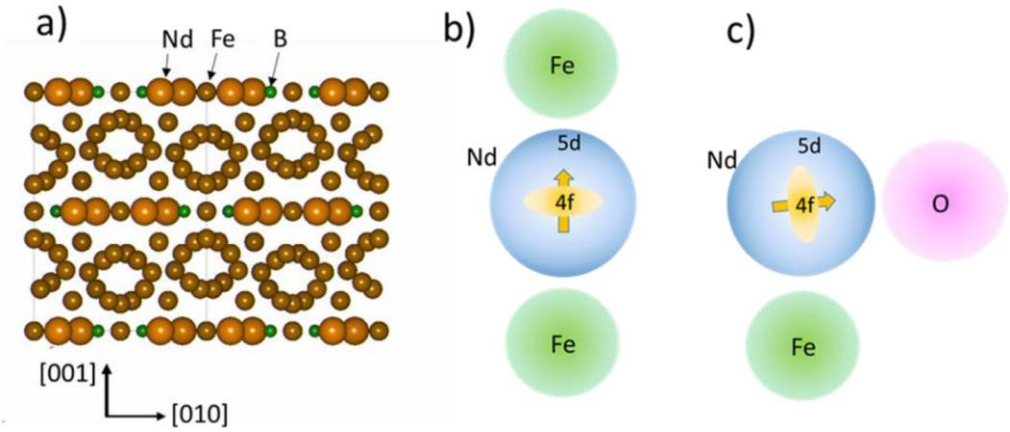

Figure 3.2 Illustrations of atomic arrangements in the $Nd_2Fe_{14}B$ crystal structure viewed along the [1 0 0] axis.

Source: Satoshi Hirosawa, M. N., and Seiji Miyashita (2017). "Perspectives for high-performance permanent magnets: applications, coercivity, and new materials." Advances in Natural Sciences: Nanoscience and Nanotechnology 8.

The figure down below illustrates unit cell of $Nd_2Fe_{14}B$ (P42/mnm space group) with four $Nd_2Fe_{14}B$ units (68 atoms) per unit cell. This is a tetragonal crystal system in the class ditetragonal dipyramidal (Herbst, Croat et al. 1984).

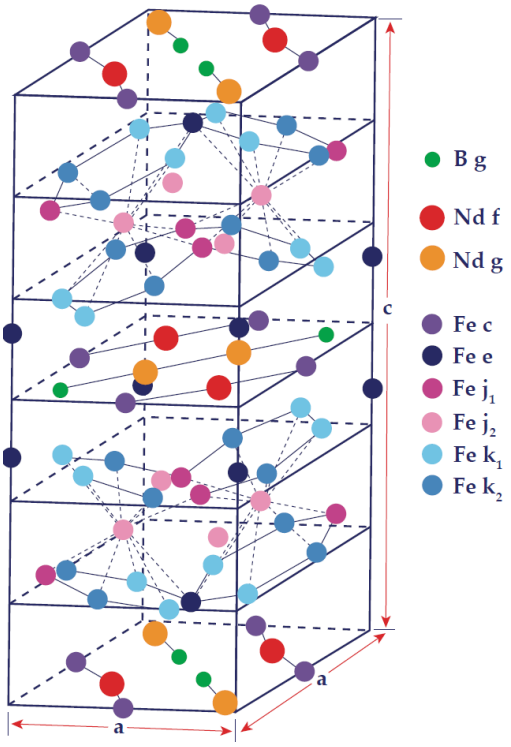

Figure 3.3 Unit Cell of $Nd_2Fe_{14}B$. The c/a ratio exaggerated to emphasize the puckering of the hexagonal iron nets.

Source: Satoshi Hirosawa, M. N., and Seiji Miyashita (2017). "Perspectives for high-performance permanent magnets: applications, coercivity, and new materials." Advances in Natural Sciences: Nanoscience and Nanotechnology 8.

The crystal structure and symmetry of $Nd_2Fe_{14}B$ result from mirror symmetry in two orthogonal planes and contribute to its strong magnetic properties. The neodymium and iron atoms are in parallel alignment within the sublattices. This symmetry produces a magnetization of approximately 1.6 T at room temperature and an anisotropy of resulting from the ‘mm’ symmetry through the two neodymium sites (Anderson 2010).

3.1.2 Polymer Bonded Magnets

Major problems with permanent magnets are their extreme brittleness and poor thermal stability which is intensified by high temperature, corrosive, and dynamic loading environments. Polymer bonded magnets (PMB) are composites with permanent magnetic powder embedded into a nonmagnetic matrix such as thermoplastic, thermoset or elastomeric binders. PBM are usually the replacement of permanent magnets in those harsh environments. The magnetic powders are typically ferrite, NdFeB, SmCo, alnico, or hybrids and binders used are nitrile rubber and vinyl, nylon, PPS, polyester, teflon, and thermoset epoxies. The mechanical properties of PBMs depend strongly on properties of the polymeric matrix, magnetic filler, and the interface in between the components. The polymeric properties allow for easy complex shapes fabrication, magnetic materials hardness, low thermal conductivity and resistance to corrosion(Xiao and Otaigbe 2000). The biggest disadvantage for PBMs is the non-magnetic binder lowers the overall density of the magnet and dilutes the properties of the magnetic particles. This generate less magnetic output per unit volume than fully dense magnets.

Injection and compression molding have become ideal manufacturing methods in the production of magnetic components with complex shapes with high accuracy at high production rates. Calendering process forms continuous strips by soften the material with heat and compressing it with large rollers. The thickness of the final product is determined by the gap between the cylinders. The process of injection molding forces the heated material through small channels into mold cavities at very high pressure. The mold is cooled and become solid before they are taken out. Magnets can be produced at high rate with complex shapes. The ratio of magnetic powder to binder is usually around 70:30.

Extrusion is the process that applies a strong force onto polymeric compound with a large screw through a heated die and controls the profile as the compound cools into a solid. Usually the magnetic powder loading of the final product is around 75% range. The abrasive nature of ferrite and rare earth alloys requires special tooling resistant wear. Another manufacturing process used in the production of bonded magnets is compression bonding. Magnetic powder is mixed with the binder, usually a thermoset epoxy, flowed into a press cavity and compacted under tremendous amount of pressure and cured at temperatures of about 150–175 °C. A major advantage of bonded magnet processing is near net shape manufacturing requiring zero or minimal finishing operations compared to powder or cast metallurgical processes. In addition, value added assemblies can be economically produced in a single operation.

3.2 Organic Based Magnets

Two different carbon systems that possess highly stable free radicals will be looked at and possibly be applied to AM; 7,7,8,8-Tetracyano-p-quinodimethane (TCNQ) polymer with organic π-conjugated network structure through self-polymerization and highly oriented pyrolytic graphite (HOPG) with the formation of ferromagnetic order through the localized defect structures.

3.2.1 7,7,8,8-Tetracyano-p-quinodimethane (TCNQ) monomer

Crystalline solids of small-molecule radicals or charge-transfer salts were the first set of organic based magnets that caught the attention of scientists because of the ferromagnetic transitions they possess at very low temperatures. The development in the field of research was sparked by the discovery of the first organic metal, a charge-transfer complex formed

by TCNQ and tetrathiafulvalene. TCNQ molecule (Fig. 3.4) was first synthesized by Acker and Hertler in 1962 from the condensation product of 1, 4-cyclohexanedione and malononitrile and is easily reduced to an anion-radical or to p-phenylenedimalononitrile(Acker and Hertler 1962).

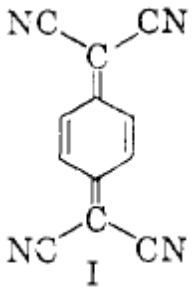

Figure 3.4 7,7,8,8-Tetracyano-p-quinodimethane (TCNQ) monomer

Source: Acker, D. S., R. J. Harder, W. R. Hertler, W. Mahler, L. R. Melby, R. E. Benson and W. E. Mochel (1960). "7,7,8,8-TETRACYANOQUINODIMETHANE AND ITS ELECTRICALLY CONDUCTING ANION-RADICAL DERIVATIVES." J. Am. Chem. Soc. 82(24): 6408--6409.

TCNQ is a strong π-acid which forms a stable, crystalline anion-radical salts of the type $M^{+}TCNQ^{-}$ and $M^{+}(TCNQ)^{-}(TCNQ)$ with high electric conductivity and magnetic properties. Because of its amazing properties, there have been interests in TCNQ and its derivatives. These donor–acceptor molecular systems exhibit a wide variety of potential applications, including molecular electronic devices, materials for non-linear optics, artificial photosynthetic systems and semiconducting materials.

3.2.2 Highly Oriented Pyrolytic Graphite (HOPG)

Graphite is a bulk material that consist of stacked graphene layers. Carbon atoms across each plane are covalently bonded in honeycomb formation (Fig. 3.5). The interaction between each adjacent plane are held together is the weak Van Der Waal bonding. This means it has different properties across different planes. The C plane (across its layers) it

has low thermal conductivity, acting as an insulator, while A-B plane (with the layers) it has very high thermal conductivity.

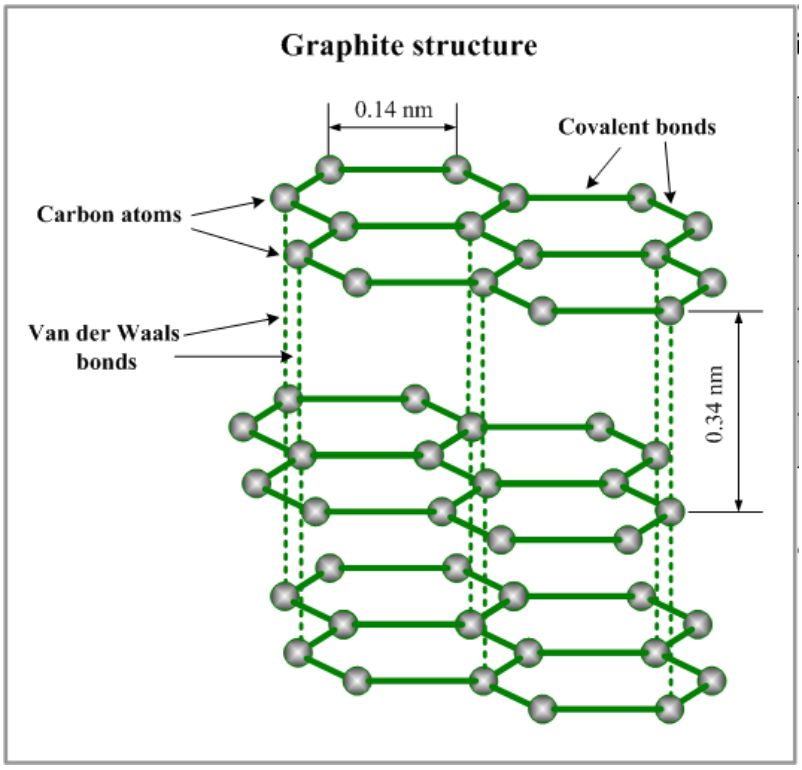

Figure 3.5 Graphite Structure.

Source: http://www.substech.com/dokuwiki/doku.php?id=graphite

Pyrolytic Graphite is a unique form of graphite manufactured by decomposition of a hydrocarbon gas at very high temperature in a vacuum furnace. The result is an ultra-pure product that is close to theoretical density and extremely anisotropic. It consists of crystallites that are relatively well aligned respect to their c-axis whereas their a-axes are randomly oriented. One dimensional single crystal has a complex microstructure. High quality HOPG was composed of domains up to 1 mm large that contained several smaller mosaic blocks with thicknesses exceeding several micrometers

Graphite have been studied extensively for a long time and still display new phenomena on the lattice surface. The defect structures in the sp^2 bonded carbon lattice

have shown great interest and have not been well characterized experimentally. Grain boundaries are one of the most commonly occurring extended defects in highly oriented pyrolytic graphite (HOPG) because of its polycrystalline character. Defects on the lattice break the electron-hole symmetry, leading to the formation of localized states at the Fermi energy. With no electron-hole symmetry, these states induce a transfer of charge between the defects and the bulk. Point defects such as vacancies and hydrogen-terminated vacancies could be magnetic(Červenka and Flipse 2009).

.

CHAPTER 4

METHOD OF SYNTHESIS

4.1 Preparation of the NdFeB Bonded Composite Filament

The NdFeB bonded composites labeled "MQIP-N270" was purchased from the Molycorp Magnequench. The composite consists of NdFeB powder embedded into the polyamide (PA)12 matrix. The "N" means it was made with MQP-B powder. "MQIP" means this was isotropic powder the was produced by MagneQuench. The MQP-B product consists Nd-Pr-Fe-B alloy composition. This blend is typical used because the supply of PrNd (neodymium (Nd), praseodymium (Pr)) is greater than Nd or Pr alone. PrNd is a natural pair of elements in rare earth (RE) deposits and needs a specialized separator to process PrNd into Nd and Pr. The magnetic performance with PrNd based magnet are comparable with the Nd or Pr based magnets. These NdFeB based powders are typically crushed to < 200µm and have an isotropic 20-30 nm nanocrystalline structure. The magnetic and physical testing properties are shown in the table below.

Table 1: Magnetic and Physical Properties of the NdFeB bonded composite

Magnetic Properties							
Remnant induction(Br)		Coercivity (Hc)		Intrinsic Coercivity(Hci)		Maximum Energy Product(BHmax)	
mT	G	kA/m	Oe	kA/m	Oe	kJ/m^3	MGOe
585	5850	370	4650	710	9700	54.1	6.8
Physical Properties							
Mold Density	MFR	Flexural Strength	Tensile Strength	Izod Impact	Moisture	Linear Expansion	Deformation Temp.
g/cm^3	(g/10 min) 270°C/5kg	MPa	MPa	kJ/m^2	ppm	1/°C	°C
5.28	505	114.3	60.3	13.1	46	3.5 E-05	151

4.2 Preparation of the Organic Based Magnetic Materials

4.2.1 Preparation and synthesis of TCNQ polymer

TCNQ (Sigma Aldric was recrystallized three times from freshly distilled acetonitrile to avoid any possible metallic contamination. TFMSA (Sigma Aldrich) was freshly distilled under reduced pressure prior to use. 5.0 g of the TCNQ crystals were taken in a three-neck round-bottomed flask under the nitrogen flow, and 30 mL of freshly distilled TFMSA was added and stirred at room temperature for 30 min. The temperature was gradually raised from 50°C to 140°C and maintained at each temperature for 1 hr. In an eight-hour period, the self-polymerization was set at 155°C where the TCNQ monomers in the trifluoromethanesulfonic acid slowly converted into a highly viscous black solid gel-like polymeric material. This organic synthesis was an aromatic cyclization of three cyano (-CN) groups in TCNQ leads to the formation of a triazine ring in the presence of TFMSA. The final product was collected and Soxhlet extracted with methanol and water successively for 3 days each to remove any possible impurity. The sample was then collected by filtration and freeze-dried at 120°C under reduced pressure for 3 days to yield a black material(Mahmood , Mahmood, Park et al. 2018).

4.2.2 Preparation of HOPG filament

To induce a magnetic response in the HOPG, there must be an introduction of defects of the surface of the graphene. There are two ways of creating point defects in graphene. The first method is applying fluorine adatoms in concentrations x gradually increasing to stoichiometric fluorographene $CF_{x=1.0.}$ The second method is the proton irradiation applied to the graphene surface. Both methods are known to create defects that carry magnetic

moments with spin 1/2. The proton irradiation method will be used because fluorine atoms on graphene have a strong tendency towards clustering because of low migration barriers

The HOPG samples were prepared by ultrasonic cleavage of high-purity HOPG in an organic solvent. At the end, the 10-50nm graphene crystallites, predominantly mono- and bilayers, are aligned parallel to each other and electronically decoupled. Once the preparation is completed, the preparation to make the graphene-based polylactic acid filament was taken from the article “3D Printed Graphene Based Energy Storage Devices”.

4.3 Filament Manufacturing

Typical FDM systems fabricate parts only with certain thermoplastics and waxes. So far, a wide range of engineering plastics such as ABS, polycarbonate (PC) and blends of ABS and PC have been developed and applied to the layer-by layer deposition of extruded material through a nozzle using feedstock filaments from a spool. Currently, a wide range of engineering plastic, metals and composites are in the developing stage and being applied to FDM process for R&D purposes or entering the commercialization stage. These new materials must meet the required size, strength and properties needed in the growing area of rapid tooling and rapid manufacturing.

Feedstock filaments for FDM machine must possess mechanical properties such as low melt viscosity, high strength, high strain and high modulus. Low melt viscosity allows the ease of flow through the nozzle and prevent back flow. Filament with good mechanical properties acts as piston for the molten end of the filament without buckling which can disrupt the printing process. This requires proper formulation and mixture of constituent materials for obtaining certain properties of the composite material so it can form into filament form so it can be used in the FDM process. Must go through the experimental

process of selecting the correct proportion of constituent materials and fillers to achieve the desired properties of the composite material.

To create filament feedstock, careful proportion of polymer, additives and fillers are premixed and subsequently compounded using a twin-screw extruder set at specific screw speed at a temperate around polymer's melting temperature. The end-product, usually pellet form, is fed into the single screw extruder where it is drawn into a filament with a thickness ranging between 1.65-1.85 mm and spooled with a winder. Enough friction on the filament provide enough force to feed it to the liquefier.

4.4 Filastruder Filament Extruder

Filastruder is a filament making machine with the ability to produce filaments for the 3D printer from polymer pellets or specialized polymeric batches. It was invented by Tim Elmore, a Mechanical Engineering PhD student at the University of Florida and his friend Allen Haynes to fulfilling the high demand of producing 3D filament and avoiding the high cost of buying expensive 3D printer filament.

The framework of the extruder is made out for aluminum 606 alloy. It has a model GF45 motor supplies 14.7 N-m torque that turn to screw to push the melt through the die. It has a Pulse Width Modulation (PWM) controller that controls the voltage (speed) and current (torque) and displays the input voltage, motor voltage, motor current, and motor power (load). Ceramic heaters and thermistors are connected to the front end the extruder, near the nozzle die to provide heat. (up to 250 C) to melt the polymer and extrude out of the hole of the die.

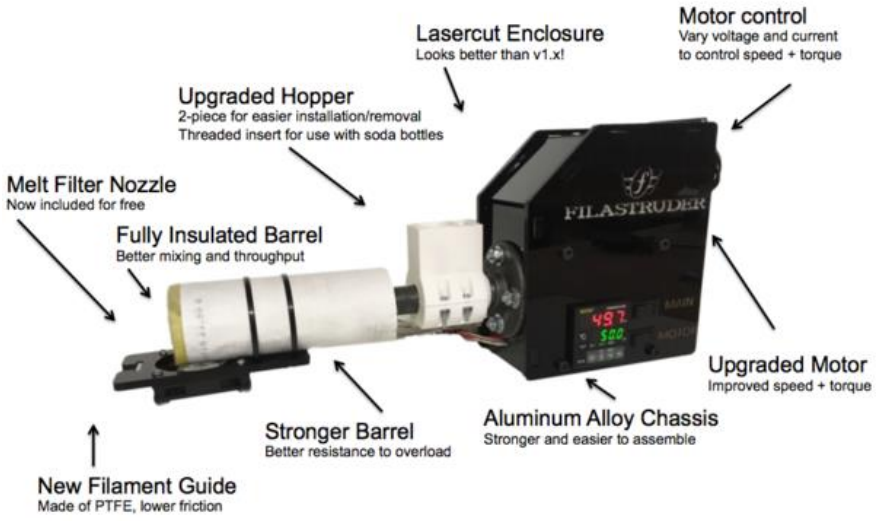

Figure 4.1 The Filastruder Filament Extruder.

Source Filastruder. "The World's Premier DIY Filament Extruder/Maker." Filastruder, www.filastruder.com/.

4.5 AM Setup and Magnetizing 3D parts

All the magnetic materials applied in this study will be printed through Fused Deposition Modeling (FDM) Setup. The FDM printing setup for the NbFeB bonded composite, which was taken Huber et.al., is shown in the table down below. The FDM printing setup of the organic magnetic material depends on the mechanical properties of the synthesized materials, result of the filament manufacturing and the process of trial and error.

Table 2 FDM printer and slicer parameter

Parameter	Value
Extruder Temp.	255C

Layer Height	0.1 mm
Printer Speed	20 mm/s
Fill Density	100%
Fill Pattern	Rectilinear
Bed Adhesion	Pritt Glue
Bed Temp.	40 C

Source Huber, C., C. Abert, F. Bruckner, M. Groenefeld, O. Muthsam, S. Schuschnigg, K. Sirak, R. Thanhoffer, I. Teliban, C. Vogler, R. Windl and D. Suess (2016). "3D print of polymer bonded rare-earth magnets, and 3D magnetic field scanning with an end-user 3D printer." Appl. Phys. Lett. 109(16): 162401.

The printed objects are typically magnetized with a pulse magnetizer using a Bitter electromagnet maximum magnetic flux density. The magnet use stacks of copper sheet metal with cooling holes and separate by insulating sheets with the same cooling hole pattern. They are arranged into a helix and then applied a large voltage across the coil. High currents flow through in a helical motion to create a uniform axial magnetic field, producing continuous magnetic fields above 10 T(Bates, Birmingham et al. 2015).

CHAPTER 5

CHARACTERIZATION TECHNIQUES

5.1 Physical and Chemical Analytical Methods

The origin of magnetism lies in the atomic level of crystalline/amorphous structure and electronic structure. Magnetic properties such as atomic moments, exchange interaction and dipolar interaction are revealed at that scale using elastic or inelastic scattering techniques on solid with beam of particle or electromagnetic radiation. Electrons and neutrons are common particle beams

5.1.1 Diffraction Methods

Diffracted methods are used to analyze crystal/amorphous structure of a solid using beam of radiation with wavelength comparable to the interatomic spacing. Electrons, nuclei, and neutrons in this region causes interference of the scattered waves which is related to the number of diffracted beams in precisely defined directions relative to the crystal axes. The mathematical description of the interference pattern is described as:

$$2d_{hkl}\sin\theta = n\lambda \quad (11)$$

Where d is the distance between the atomic plane, θ is the angle the diffracted beam, n is the number of interference and λ is the wavelength of the beam. The intensities of reflections depend on the strength of the atomic scattering and the arrangement of atoms within the unit cell.

X-ray diffraction (XRD) is a popular technique for crystal structure analysis. It's used to measure the average spacings of a group of atoms, determines the orientation of a

single crystal or grain and find crystal structure of a novel or unknown material. For X-ray operating machine, a special target on a metal is bombarded with energetic electrons at high velocity emitting characteristic x-ray radiation as electrons from the outer shell fill the holes in the inner shells. The charge of electrons causes the X-ray to scatter proportional to the Fourier transform of atomic charge distribution $\rho(r)$ which is related to the atomic number Z.

Neutron diffraction is commonly used for magnetic microstructure analysis. High energy protons from an accelerator directly impact a heavy-metal target releasing neutrons. Weak scattering of neutrons unto solids means larger sample six compared to the X-ray method. Sample preparation are typically in powder form. The crystalline powder are randomly oriented to incident beam cones correspond to a particular Bragg reflection. Set the end of the cone is a detector that measures the intensity of the diffracted beam.

5.1.2 Spectroscopic Methods

Spectroscopy is the study of how matter interacts with applied electromagnetic radiation. Spectroscopic methods are used to analyze molecular structure, composition and vibration frequencies. These methods are classified by different sections of electromagnetic spectrum such as x-ray, infrared, microwave, ultraviolet and light to identify microstructure, atomic energy levels and excitation of magnetic solid.

Transmission electron Spectroscopy (TEM) works on the same optical principles as light microscopy but uses electrons to illuminate the sample. The transmission of electrons through the sample gives TEM a greater image resolution because the wavelength of electrons is much smaller than that of photons (2.5 pm at 200 keV). These energetic

electrons provide valuable information about the material's composition, crystal structure, and morphology. Sample is placed inside a vacuum chamber where it interacts with high energy electrons to produce high nanoscale resolution surface images. The lighter regions represent a greater number of electrons passing through the sample while the darker regions are electrons flection from the sample's dense regions. The sample need to be thinly sliced for enough electrons to pass through and able to withstand the chamber's environment.

Scanning electron microscope (SEM) method is based on the scattering of electrons from the focused high energy electrons applied to the sample revealing information about the surface texture, chemical composition, and crystalline structure. It's well known for its microscale resolution range with greater magnification and depth of field than light microscopy. The sample's electron interaction creates signals including secondary electrons (produce SEM images), backscattered electrons, photons and phonons. The secondary and backscattered electrons create the surface imagers with backscattered electrons revealing more contrast to multiphase regions. Characteristic X-ray created for inelastic collisions of electron-electron interactions provides elemental analysis. Energy Dispersive X-Ray Spectroscopy (EDS or EDX) is a chemical analysis technique used alongside with scanning electron microscopy (SEM) to detects x-rays emitted from the sample during beam bombardment to characterize the elemental composition of the analyzed volume.

Hyperfine interactions of atoms in different crystallographic and molecular structure reveal the origin of magnetic and electric field. Hyperfine coupling is the result of the interaction between the magnetic moments from both the nucleus and electrons spins in atoms. The two main spectroscopic techniques for measuring hyperfine interactions are

NMR and Mossbauer spectroscopy. NMR involves resonant absorption of radiofrequency radiation by the nucleus in its ground state. Mossbauer spectroscopy involves a γ -ray transition from a nuclear excited state to the ground state, where the excited state is populated by a radioactive precursor(Coey 2010).

Scanning Tunneling Microscopy (STM) and *atomic force microscopy* (AFM) are part of scanning probe microscopy (SPM) family that provide surface analysis with demonstrated resolution on the order of fractions of a nanometer. A sharp tip is raster-scanned over a surface using a feedback loop to adjust parameters needed to image a surface. Attached to the tip is the cantilever beam that motions across the sample at measurable distances (10-4 A) picking up forces that can be as small as 10-18 N. The masses involved in the other techniques are too large to reach this value. STM huge disadvantage is it can only image conducting or semiconducting surfaces. AFM is capable of imaging almost any type of surface, including polymers, ceramics, composites, glass, and biological samples

Electrostatic Force Microscopy (EFM) is a specific type of ATM technique that scans the sample surface by measuring the electrostatic force between the surface and a biased AFM cantilever. The images produce contain electric properties such as the surface potential and charge distribution. It maps out locally charged domains on the sample surface, similar to how MFM plots the magnetic domains of the sample surface. The magnitude of the deflection, proportional to the charge density

X-ray Absorption Spectroscopy (XPS) is a surface-sensitive technique normally applied to a wide range of materials to provide quantitative and electronic information about the sample's surface. Similar to SEM/EDS technique, XPS uses a finely focused

electron beam to produce surface and compositional analysis, however, its depth analysis is less than 5nm making the method suitable for ultra-thin samples. This technique is commonly use in the developing field of spintronics. Regular electronic components utilize electron's charge to store data while devices embedded with spintronics exploits the spins of electron as the data carrier. *X-ray photoemission spectroscopy* is a surface analysis technique that provides quantitative and chemical state information at average depth of analysis of approximately 5 nm.

Two common techniques in the X-ray absorption family are extended X-ray absorption fine structure (EXAFS) and X-ray magnetic circular dichroism (XMCD). EXAFS is technique that produces diffraction patterns from interference of the outgoing and backscattered electron waves to probe the local environment of the surrounding absorbing atom, including nearest-neighbor positions, average interatomic distances and coordination number. X-ray magnetic circular dichroism (XMCD) spectroscopy is a measure the difference in absorption of left- and right-circularly polarized X-rays by a magnetized sample, often at cryogenic temperatures

Solid-state electron spin resonance (ESR) spectroscopy analysis material with paramagnetic properties possess unpaired electrons that can go through transitions of different spin states induced by external magnetic field. A resulting absorption spectrum is produced called electron spin resonance and is used to study how radical electrons are created in solid materials. This technique is comparable to those of nuclear magnetic resonance spectroscopy, but it is the electron spins that are excited instead of the spins of atomic nuclei which is ideal for studying metal complexes or organic radicals. The

electromagnetic radiation used by NMR is in the radio frequency range between 300 and 1000 MHz, while ESR is typically performed using microwaves in the 3–400 GHz range.

The g factor is the most important parameter for the description of the spin system. By keeping the electromagnetic radiation frequency constant and scanning with a strong magnetic field, a peak of absorption will occur when the magnetic field align with the two spin states so that their energy difference matches the energy of the radiation. In spin magnetism, the electron has a rotating sphere of mass m_e and charge $-e$. From the quantum mechanical description of the electron, the g-factor of the free electron is 2.00280 (Pickard and Mauri 2002).

Particle induced X-ray emission (PIXE) is technique use to analyze the sample's element and impurity concentration. With the application of an ion beam, PIXE measures the radiation emitted by electron state changes and identifies each element based on its unique emissions recorded as a spectral peak. This is an extremely useful non-destructive analytical method the analyzes samples either in or outside of a vacuum. *Low energy ion scattering* (LEIS) is typically used for identifying surface impurity concentration. Similar to PIXE but the beam of ions is scattered by a surface and not the bulk of the sample. The kinetic energy of the elastic scattering of ions produce measured peaks corresponds to atoms at the surface of the sample, caused by the momentum transfer between the incident ion and atom.

5.2 Thermal Analysis

5.2.1. Thermogravimetric analysis (TGA)

TGA measures the weight change of a material as a function increasing temperature isothermally as a function of time, in an atmosphere of nitrogen, helium, air, , or in vacuum. Its typically equipped with a mass spectrometer to identify and measure the vapors generated. Wide range of material analysis such as Inorganic materials, metals, polymers and plastics, ceramics, glasses, and composite. Sample weight can range from 1 mg to 150 mg with weight change sensitivity of 0.01 mg.

5.2.2. Thermomechanical analysis (TMA)

TMA is a technique that measures the sample displacement as a function of temperature, time and applied force. Specifically, it analyzes the changes in the free volume of a polymer and characterize linear expansion, glass transitions, and softening points of materials by applying a constant force to a specimen while varying temperature. (Tg).

5.3 Magnetic Analysis

5.3.1 Stray-field methods

Magnetic force microscopy (MFM) is a unique operation of AFM the employs a magnetic probe close to a sample and register the magnetic stray fields at the surface of the sample. Strength of the local magnetostatic interaction causes deflections of cantilever with the microscopic tip coated with ferromagnetic film. As it scans across the sample's surface the change of the mechanical resonance frequency gives an image of the stray field gradient.

Scanning electron microscopy with polarization analysis (SEMPA) analyze the spin polarization of the secondary electrons can be monitored as the electron beam is rastered across the surface. This give rise to the net spin density of the material which is relates to its magnetization.

5.3.2 Magneto-optic and electron-optic methods

Magnetic-optic studies the influence on the beam of radiation as it passes through the magnetic ordering of the sample. The spin orbit coupling dictates these optic effects which can be scale to magnetization M(r) and is more pronounced with heavier atoms.

Faraday effect occurs when plane-polarized light passes through a thin, ferromagnetic, transparent sample and rotates the plane of polarization. This phenomenon is applied in the analysis of spin polarization in organic electronics and the domains of transparent ferrimagnets. Kerr effect is another phenomenon that occurs from light reflection off the magnetic surface of the sample which created a change in polarization and reflection of intensity of the light.

5.3.3 Bulk Magnetization Measurements

The magnetometer works by vibrating a sample verticality at the midpoint of the field produced by a magnet When a magnetized sample is vibrated, an electric current, proportional to the magnetic moment is induced in the pickup coils placed near the vibrating sample. The induced current has the same frequency as the vibration frequency of the sample (Grössinger 2008)

The *superconducting quantum interference device* (SQUID) is a powerful tool that consists of two superconductors separated by thin insulating layers to form two parallel

Josephson junctions. The sample moves through a system of superconducting coils that are connected to the SQUID with superconducting wires.(Grössinger 2008)As a magnetometer, it is capable of detecting small changes in the magnetic fields. The Josephson junction is separated by an insulating layer that is so thin that electrons can pass through allowing superposition, where each electron moves simultaneously in both directions.

Hysteresigraph or permeameter designed to measure B(H) loops where H is the internal field in the sample. For materials which cannot be saturated in the field of the electromagnet (≈2 T), the sample may be first saturated along its axis in a pulsed field, and then transferred to the hysteresigraph for measurement of the demagnetizing curve in the second quadrant.

5.3.4 3D Magnetic Scanner System

3D Magnetic Scanner System, which consist of a hall sensor and microcontroller, will be setup onto the 3D printer to measure the magnetic flux density of the printed objects. The purpose of this system is to avoid the complex sensor system the requires exact positioning and alignment of the sensor. The 3D Hall sensor was used to detect the magnetic flux density created by the object. The programmable microcontroller read out the components of B at a specific frequency, measurement range, and a measured detectivity of 40 $\mu T/(Hz)^{1/2}$ for DC magnetic fields. This system setup was provided by the work of Huber et al. (Huber, Abert et al. 2016).

Hall effect is development of a voltage across a conductive sheet as current is flowing and the sheet is under the influence of a magnetic field. The electrons in the sheet drift under the influence of an applied external magnetic field. The force acting on the

electrons is proportional to its velocity and density of the flux and causing imbalance of charge to across the edges of the conductive strip. This produce transverse electric field which produce output voltage across the conductor which is proportional to the magnetic field strength it detects.

Hall effect sensors require signal conditioning, so it can be used in most application. Installed typically inside a sensor is the amplifier and temperature regulator as shown in the Fig. 28 below. Voltage regulation is also needed when operating from an unregulated power supply. The Hall voltage is a low-level signal in the magnitude of microvolts in the presence of about one gauss magnetic field. This is why a differential amplifier is necessary for this low-level output to produce a low noise, high input impedance and moderate gain.

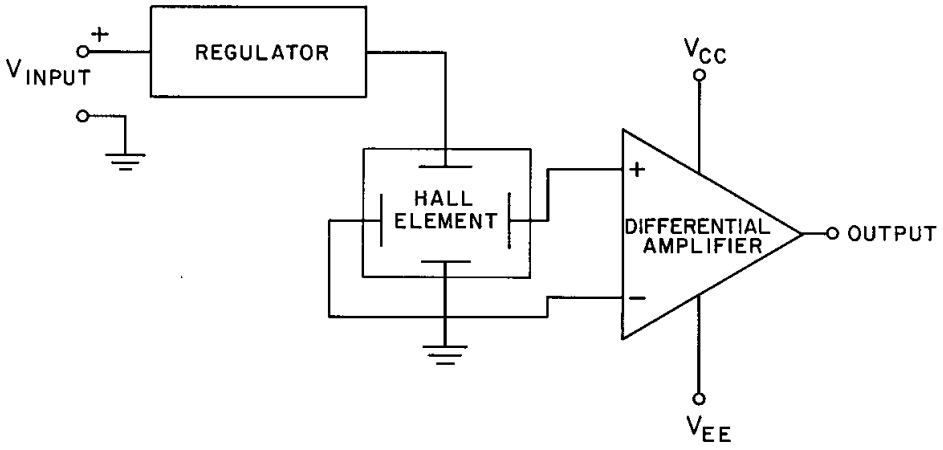

Figure 5.1 Basic Hall Effect Sensor.

Source: Hall Effect Sensing and Application (2010). Retrieved from https://sensing.honeywell.com/hallbook.pdf

Connected to sensor is the microcontroller, a compact integrated circuit designed to perform a specific operation in an embedded system. A typical microcontroller includes a processor, memory and input/output (I/O) peripherals on a single chip. These devices are

designed to be robust and self-sufficient without any additional computing components because they hold enough onboard memory as well as offering pins for general I/O operations, so they can directly interface with sensors and other components. Microcontrollers are programmed typically with higher-level languages such as C++ or Java with the assistance of the integrated development environment (IDE), an essential tool needed to program a microcontroller.

Calibration process of the 3D magnetic scanner system involves the use of a predefined magnetic object. The inhomogeneous reference field is created which relates to the geometric shape of the object sample and the stray field it produces. The scanner detects the magnetic field of a defined volume outside the magnetic object. By representing the reference field as the numerical solution B_s and the measured field as B_m, an optimization problem can be formulated, to minimize the squared error between the calculated and measured values so the calibration parameters can be determined. The reference field of a cylinder magnet can be calculated numerically by using the magnetic potential $\Phi(r)$ as shown below:

$$B_s(r) = -\mu_0 \nabla \Phi \tag{12}$$

μ_0 and M represent vacuum permeability and the magnetization.

The experimental field B_{exp} is extracted from the measurement data $B_m(r)$and background field $B_{back}(r)$ using the equation $B_{exp} = B_m(r) - B_{back}(r)$. The any possible magnetic field inference outside the experiment is removed to form a baseline measurement and reduce calculation errors. The simulated field B_{sim} relates to the calibration parameters for the sensor *s, γ, β, α, Δr* as shown in the equation below:

$$\beta_{sim} = s \cdot R_{zyx}(\gamma, \beta, \alpha) \cdot \beta_s(r - \Delta r) \tag{13}$$

Where s is the sensitivity of the Hall sensor, $\mathbf{R}_{ZY\,X}$ represent the rotation matrix with the Euler angles ($\gamma, \beta, \alpha,$) to compensate the tilting of the sensor Δr is the sensor offset. Solving the following minimization problem results in the unknown parameters of the calibration:

$$\min_{s,\gamma,\beta,\alpha,\Delta r} = \left\|B_{exp} - B_{sim}\right\|^2 \tag{14}$$

The figure below demonstrates a significant difference between simulation and measurement in Part a. Part b shows the application of the calibration procedure seem to work very well with the simulation after the calibration method.

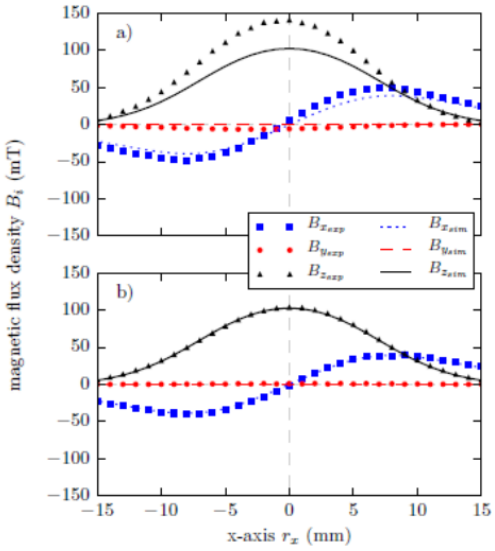

Figure 5.2 Illustrate the difference between simulation and measurement after applying the calibration procedure.

Source: Huber, C., C. Abert, F. Bruckner, M. Groenefeld, O. Muthsam, S. Schuschnigg, K. Sirak, R. Thanhoffer, I. Teliban, C. Vogler, R. Windl and D. Suess (2016). "3D print of polymer bonded rare-earth magnets, and 3D magnetic field scanning with an end-user 3D printer." Appl. Phys. Lett. 109(16): 162401.

5.4 Numerical Method: FEM Analysis

The Maxell equations are a set of differential equations mathematically the interaction between the between electric and magnetic field, charge and currents. It predicts electromagnetic phenomena and used in a variety of applications to solve complex problems. For example, numerical method is used to analyze waveguide structure. These are structures that guide waves, such as electromagnetic wave of sounds, with low energy by limit expansion to 1D or 2D, similar to how a canal restrict the flow of water in one direction.

When magnet produces H-field with no conduction current, H can be expressed as a magnetic scalar potential φ:

$$H = -\nabla\varphi_m \tag{15}$$

Φm have units in ampere. Scalar potential satisfies Poisson equation

$$\nabla^2\varphi_{\mathrm{m}} = -\rho_{\mathrm{m}} = \nabla \cdot \mathrm{M} \tag{16}$$

Where the magnetic charge density ρ_m. When conduction currents is involved the vector potential is used:

$$\nabla^2\mathrm{A} + \mu_0\nabla \times \mathrm{M} = \mu_0\mathrm{j} \tag{17}$$

There are two methods, finite difference and finite element, use to solve second order differential equation involving potential, Finite difference, estimate solutions valid at a collection of points within the region of interest. Finite element approximate solutions by divide up the region into a mesh of 3D cells. The first step of numerical computation is the preprocessing stage where the geometry of the object is defined, and material properties

are inputted. Next step is the numerical solution to the potential problem. The final step, forces and field analysis can be extracted from the numerical solutions (Virjoghe, Enescu et al. 2012).

5.5 Computational Analysis

Design of novel ferromagnetic system requires the understanding of the complex inter-radical exchange interactions. Quantum mechanics was essential to the quantitative analysis of the ferromagnetic interaction. It was the matrix form of quantum mechanics by Heisenberg and Born, the alternative but equivalent wave-mechanical form by de Broglie and Schrodinger, and the introduction of electron spin by Uhlenbeck and Goudsmit that shape our understanding of magnetism today (Van Vleck 1978). Quantum mechanics uses approximation methods of Schrodinger equation to describes molecules in terms of interactions among nuclei and electrons, and molecular geometry in terms of minimum energy arrangements of nuclei to predict structures, energetics, reactivities and other complexities of molecules. The increase in computing power and speed and designs of efficient quantum chemical algorithms have been key to its developments. It has replaced difficult, expensive, dangerous and time-consuming chemical experiments. However, it not used as a replacement of experimental studies, but it allows chemist understanding known chemistry and explore new or unknown chemistry.

Ab initio quantum chemistry is one of the many computational methods that uses computers to perform chemical analysis based on established laws of nature. Ab initio means “from the beginning” or “from first principles”. This powerful molecular modeling tool have over the decades shown its ability to calculate the electronic energy, electron

density, and other properties with a well-defined, automated approximation. There are several methods that perform calculations for reaction mechanism of open-shell systems.

Open-shell elongation method was developed as a linear-scaling method that mimics the polymerization reaction using a computer. Open-shell fragment molecular orbital method is typically use for calculating large systems. In this method, properties such as the total energy of the system can be obtained from the energies of each fragment and fragment pair. Density matrix renormalization (DMRG) methods are among the most actively developing ab initio QC techniques used to predict magnetic properties,

Density functional theory (DFT) is another computational method that stems from the properties of the molecule based on a determination of the electron density of the molecule. It is used today to investigate the structural, magnetic and electronic properties of molecules, materials and defects. Electron density, unlike wavefunction that is a mathematical construct and not a physical reality, is a physical characteristic of all molecules. A functional is defined as a function of a function, and the energy of the molecule is a functional of the electron density. Many-body electronic wavefunction is the complex function of 3N variables (the coordinates of all N atoms in the system) , while electron density is only a function of x, y, z positions of the electrons (Capelle 2002).

There are three types of DFT methods. Local density approximation (LDA) methods assume uniformity of density within the molecule which make it not a very popular or useful method. Gradient corrected (GC) methods take into account the non-uniformity of the electron density. Third DFT methods is the hybrid approach of incorporating some of the more useful features from ab initio methods (specifically Hartree-Fock methods) with some of the improvements of DFT mathematics

DFT methods, unlike ab initio methods, can be used for calculations involving metals. Hybrid methods, such as B3LYP, are often the method of choice for reaction calculations. Some DFT methods are specifically designed for specific applications, such as the MPW1K hybrid method, designed for determination of kinetics problems. the most popular software packages, including Gaussian, GAMESS, HyperChem, and Spartan.

CHAPTER 6

RESULTS

6.1 Analysis of NdFeB and NdFeB Bonded Composite in AM

NdFeB has the best overall magnetic performance in the classes of hard magnets. (B_r over 1 T, H_c above 1000 kA/m, $(BH)_{max}$ larger than 200 kJ/m^3). However, there is an increasing reliance on the limited rare earth supply cause by increasing demand from this rapidly developing technological world. The next development steps for NdFeB production are the fabrication of complex shape, near net shape manufacturing and magnetic stability at elevated temperatures up to 200° C.

Jaćimović et al. conducted the first 3D fabrication of net shape NdFeB magnets using Selective Laser Melting (SLM) technique. This fabrication delivers the design freedom of the magnet's shape and precise control of its internal microstructure. The images below illustrated two shapes with different texture fabricated by the SLM printer, Model Realizer SLM 50. It succeeded in creating magnets with intricate designs at a small scale, which is difficult to accomplish with other fabrication processes.

Figure 6.1 The photograph of printed magnets of various shapes. The left object, expanded view on the bottom image, demonstrate the full power of 3D printing very complex shape, a novel functionality to the hard magnets.

Source: Jaćimović, J., F. Binda, L. G. Herrmann, F. Greuter, J. Genta, M. Calvo, T. Tomše and R. A. Simon (2017). "Net Shape 3D Printed NdFeB Permanent Magnet." Adv. Eng. Mater. 19(8): 1700098.

A powerful laser beam was applied to melts and fuses the magnetic powders together layer by layer. There was five laser settings (laser power, laser focus, point distance, exposure time and hatching distance) for the pulsed Nd:YAG-Laser with the energy output set at 120 W to melt the powders to its final stable form. Because NdFeB alloy are known to be very fragile, it was important to have the right printing parameters to produce fully functional dense quality magnets. The printing procedure was conducted under argon gas with an oxygen level below 500 ppm.

The printed samples obtained very good magnetic properties, as shown in the magnetic hysteresis loop below, without additional post heating treatment: H_c = 695 kA/m, B_r = 0.59 T, $(BH)_{max}$=45 kJ/m^3. 5 x 5 x 5 mm^3 cubes were produced with 50 μm long microcracks detected and with a good average density of 4.67 g/cm^3. To demonstrate the full potential of 3D printing complex shapes, channels were successfully printed inside the object for possible cooling paths.

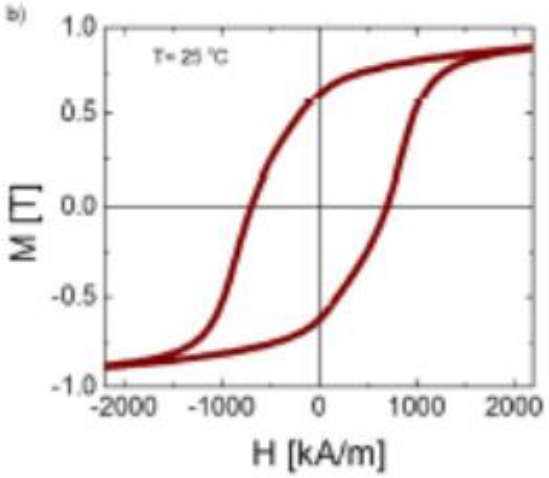

Figure 6.2 Full magnetic hysteresis loop of NdFeB magnet using SLM method

Source: Jaćimović, J., F. Binda, L. G. Herrmann, F. Greuter, J. Genta, M. Calvo, T. Tomše and R. A. Simon (2017). "Net Shape 3D Printed NdFeB Permanent Magnet." Adv. Eng. Mater. 19(8): 1700098.

The first SEM image in Fig. 6.3 corresponds to a cross section of a 3D printed specimen under slow solidication with measurements of H_c=10 kA/m, B_r= 0.05 T, and $(BH)_{max}$ of only 0.1 kJ/m^3. The laser was programmed took a slow path away from the deep penetrated (100 μm) liquid pool created causing a slow solidification process. The EDX mapping and XRD analysis identified three different phases on the sample's cross section. The small white regions with average diameter of few hundreds of nanometers correspond to the formation of neodymium oxide from the interaction of residual oxygen inside the printing chamber. The other two phases consist of Fe and $Nd_2Fe_{14}B$, in dark and light grey colors, respectively. Iron present in the matrix of $Nd_2Fe_{14}B$ meant there was a reduction of the overall volume percentage of the hard-magnetic phase and which leads to a reduced

remanence. The total coercivity was also reduced because the soft magnetic iron acting as the center of reversed magnetic domain in the hard magnetic phase.

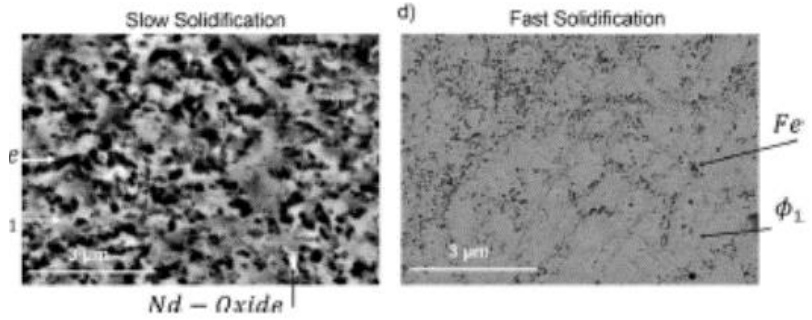

Figure 6.3 SEM picture of the printed sample with slow solidification on the left and fast solidification on the right side.

Source: Jaćimović, J., F. Binda, L. G. Herrmann, F. Greuter, J. Genta, M. Calvo, T. Tomše and R. A. Simon (2017). "Net Shape 3D Printed NdFeB Permanent Magnet." Adv. Eng. Mater. 19(8): 1700098.

The second SEM image represent the cross section of a sample with better magnetic properties of H_c = 695 kA/m, B_r = 0.59 T, and $(BH)_{max}$ = 45 kJ/m^3. This sample went through rapid solidification as the laser beam was set move a little faster (100 µs) away from the liquid melt. Powder additives like Co, Zr and Ti also played an important role in the stabilization of the growth of the target magnetic phase (light grey region). The laser power and deposited powder layer thickness of 20 µm led to a much thinner liquid melt pool (20-30 µm), with direct contact with the solidified material underneath. Small iron segregations (dark grey regions) were observed in the image, but with lower concentration than the slow solidified samples. The magnetic characteristics of the printed samples have shown to outperform injection molded and SPS sintered magnets composed of the same powder Fig. 6.4.

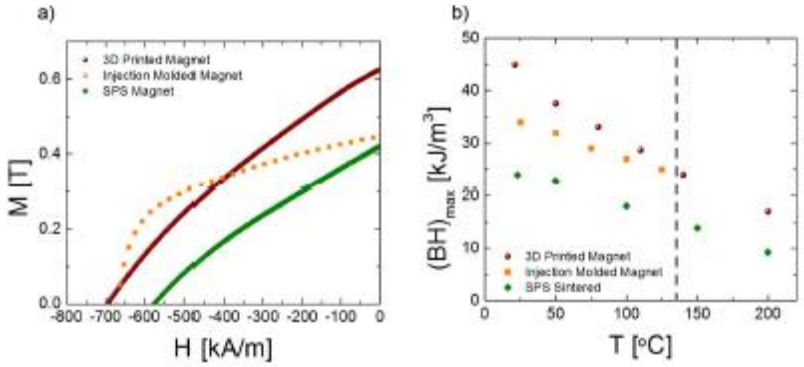

Figure 6.4 a) Magnetization as the function of demagnetizing field for three different samples, all based on the same MQP – S powder: 3D printed, Injected molded magnet with most used PA 12 polymer, and SPS sintered. b) Temperature dependence of the (BH)max for the same three samples.

Source: Jaćimović, J., F. Binda, L. G. Herrmann, F. Greuter, J. Genta, M. Calvo, T. Tomše and R. A. Simon (2017). "Net Shape 3D Printed NdFeB Permanent Magnet." Adv. Eng. Mater. 19(8): 1700098.

Bonded NdFeB magnets are typically prepared by mixing magnetic powder with binder followed by compacting or molding the material to final shape. Table 3 below shows sintered NdFeB magnets with magnetic properties that outperforms polymer bonded NdFeB and SLM magnets. Sintered NdFeB magnets are typically made by using sintering process temperature in absence of oxygen. Bonded NdFeB magnets are prepared by mix together magnetic powder with binder followed by the compacting or molding process giving the material its final shape. The sintered NdFeB magnet, with high density and well-defined internal microstructure, has higher magnetic properties than the bonded NdFeB magnet or SLM magnets.

Table 3 Comparting magnetic properties of bonded, sintered and SLM magnets

Magnetic Properties of NdFeB magnets			
Paper	Bonded NdFeB	Sintered NdFeB	SLM Magnets
Remanence Br (kG)	6.9	13.1	5.9
Energy Product BHmax (MGOe)	10	42	5.7
Coercivity Hci (kOe)	9	14	8.7
Curie Temperature Tc (C)	200	310	N/A

Source: Suprapedi, P. Sardjono and Muljadi (2016). "Physical and magnetic properties, microstructure of bonded magnet NdFeB prepared by using synthesis rubber." J. Phys. Conf. Ser. 776(1): 012015.

Sintered NdFeB magnets have disadvantages such as low oxidation and corrosion resistance at room temperature and mechanical properties not suitable for many applications. Bonded NdFeB permanent magnets, mainly composed of NdFeB magnetic powder and various types of polymeric binders, have the advantages of low weight, corrosion resistance, easy machining ability, forming and handling, high production rate. Suprapedi et al. conducted research on the effect of the polymer composition as binder on NdFeB by testing the physical properties, microstructure and magnetic properties of four different fractions of NdFeB powder and binder: 1) 97 wt.% of NdFeB (NQP-B) and 3 wt.% of rubber, 2) 95wt.% of NdFeB (NQP-B) and 5 wt.% of rubber, 3) 93 wt.% of NdFeB (NQP-B) and 7 wt.% of rubber, 4) 91 wt.% of NdFeB (NQP-B) and 9 wt.% of rubber. The goal of this experiment was to understand the influence of rubber composition to density and magnetic properties on preparation of bonded NdFeB magnet.

Suprapedi et al. demonstrates how the increase of the rubber content reduces both the overall magnetic field and density. The bulk density value has tendency decreasing when rubber composition increases, because the density of rubber is lower than density of NdFeB powder. Also, the theoretical density of bonded magnet NdFeB is about 5 – 6 g/cm^3 but the densification of the sample bonded NdFeB magnets was around 70-80% due to the

low pressure on forming process (30 MPa). The addition of rubber material are less dense than NdFeB magnets. A decrease in density and magnetic powder decreases the magnetic properties. The NdFeB content for the SLM magnets was very close to 100% before and after the printer.

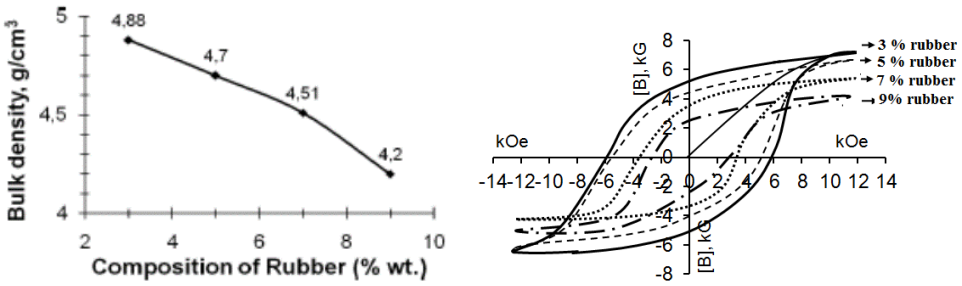

Figure 6.5 The curve of bulk density Nd2Fe$_{14}$B and BH-curve of bonded Nd$_2$Fe$_{14}$B magnet for different rubber composition

Source: Suprapedi, P. Sardjono and Muljadi (2016). "Physical and magnetic properties, microstructure of bonded magnet NdFeB prepared by using synthesis rubber." J. Phys. Conf. Ser. 776(1): 012015.

The next set of SEM images below illustrate the samples bonded magnet made by using 3 to 9 % wt with the polymer binding all surface of grains. can be seen that the rubber binds all surface of grains. The grey color represents the grain of magnetic Nd$_2$Fe$_{14}$B and the white and black color indicate as rubber polymer. The 7% and 9 % of rubber show that the polymer rubber seem to bind to the grain boundaries and grains surface while polymer on sample with 5 % and 3 % of rubber bind to the grain boundary.

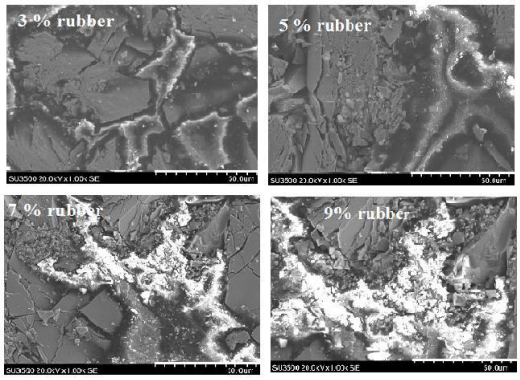

Figure 6.6 SEM images of samples bonded magnet NdFeB with variation of rubber binder.

Source: Suprapedi, P. Sardjono and Muljadi (2016). "Physical and magnetic properties, microstructure of bonded magnet NdFeB prepared by using synthesis rubber." J. Phys. Conf. Ser. 776(1): 012015.

From the research paper “Big Area Additive Manufacturing of High Performance Bonded NdFeB Magnets” the group was able to fabricate, using the Big Area Additive Manufacturing (BAAM) machine, near-net-shape NdFeB bonded magnets with magnetic and mechanical properties comparable to the traditional injection molded magnets. The magnetic filament consists 65 wt.% NdFeB isotropic powder (MQP-S-11-9) particles inside a PA12 matrix.

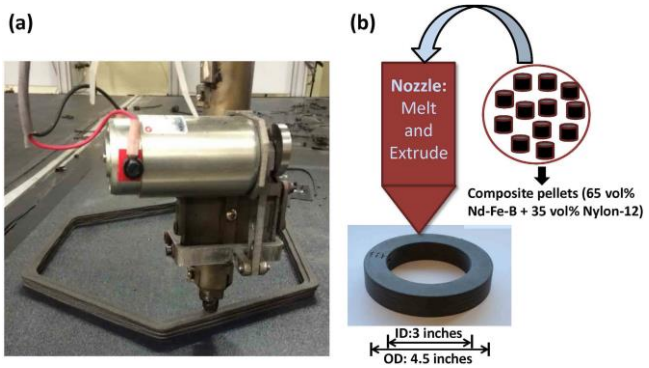

Figure 6.7 (a) Image of the nozzle depositing layers of magnetic materials on the print bed; (b) Schematic of the melt and extrude process, right underneath the nozzle is a printed magnet in a hollow cylinder shape.

Source: Li, L., A. Tirado, I. C. Nlebedim, O. Rios, B. Post, V. Kunc, R. R. Lowden, E. Lara-Curzio, R. Fredette, J. Ormerod, T. A. Lograsso and M. P. Paranthaman (2016). "Big Area Additive Manufacturing of High Performance Bonded NdFeB Magnets." Sci Rep 6: 36212.

The magnetic properties of the BAAM magnet: intrinsic coercivity (H_{ci}) = 688.4 kA/m, remanence (B_r)= 0.51 T and energy product ($(BH)_{max}$) = 43.49 kJ/m^3 (5.47 MGOe). The results are similar to the SLM magnet even with the 35% wt.% binder. The magnetic properties of the BAAM magnet did not degrade compared to the starting pellets. The SLM magnetic properties under went some changes due to phase changes

The figure below is SEM analysis of the NdFeB bonded composite before and after the 3D print. The red circles on the third image shows the fracture surfaces indicate failure which is primarily related to the debonding of the magnetic particles from the polymer binder. This is due to the increase of pressure at high temperature as the composite flow through the tiny nozzle as it is laid onto the bed platform.

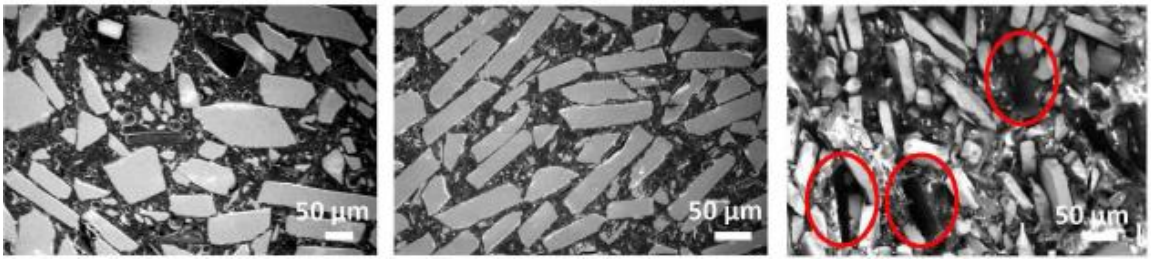

Figure 6.8 SEM micrographs. The first image is the starting composite pellets. The second image is the BAAM printed bonded magnets. The third shows the fractured surface of the BAAM magnets after tensile testing.

Source: Li, L., A. Tirado, I. C. Nlebedim, O. Rios, B. Post, V. Kunc, R. R. Lowden, E. Lara-Curzio, R. Fredette, J. Ormerod, T. A. Lograsso and M. P. Paranthaman (2016). "Big Area Additive Manufacturing of High Performance Bonded NdFeB Magnets." Sci Rep 6: 36212.

Magnetostatic energy is stored inside of magnets in a useful form. When there is no current, the magnetostatic energy contributions can be calculated by applying the integral to the volume of the magnetic object and splitting up the internal and external field. External magnetostatic energy is calculated to be:

$$E_A = -\frac{1}{2}\int_1 B \cdot HdV \quad (18)$$

This means the energy product (BH) = $2E_A/V$ is twice the energy in the stray field of magnet. When the magnetic flux B =μ_0(H + M) and the induced field H = -NM, the equation above shows the energy product have shape-dependent of magnets:

$$(BH) = \mu_0 N(1-N)M_s^2 \quad (19)$$

Huber et al. applied FDM printing to NdFeB bonded composite to make magnets with specific pre-determined shape to create a controlled magnetic field. Specific geometric shape is hard to fabricate with techniques like injection molding.

Calibrated 3D magnetic field scanner was attached to the printer and used to measure the stray field of the printed objects. Pulsed Field Magnetometry (PFM) performed the hysteresis measurements in 3D to analysis magnetic field within the printed layered structure. The samples display isotropic behavior. The measured remanence B_r, the intrinsic coercivity H_{cj} , and the volumetric mass density ϱ of the samples are listed in the illustration below.

Procedure	ϱ (g/cm^3)	B_r (mT)	H_{cj} (kA/m)
datasheet	4.35	400	630
3D print	3.57	310	740
inj. mold.	4.35	387	771

Figure 6.9 Magnetic properties from data sheet, NdFeB bonded composite and 3D printed magnet.

Source: Huber, C., C. Abert, F. Bruckner, M. Groenefeld, O. Muthsam, S. Schuschnigg, K. Sirak, R. Thanhoffer, I. Teliban, C. Vogler, R. Windl and D. Suess (2016). "3D print of polymer bonded rare-earth magnets, and 3D magnetic field scanning with an end-user 3D printer." Appl. Phys. Lett. 109(16): 162401.

This SEM image of the cross section of the NdFeB filament was produce by Huber et al. The NdFeB grains with uniaxial magnetocrystalline anisotropy mixed into the PA11

matrix. Due to the random orientation of the NdFeB grains in the matrix leads to the isotropic magnetic properties of the bulk magnet. Typically, the average number diameter of the grains can be obtained from SEM imags by using an image analysis software such as SigmaScan PRO to take the average measurements at least 300 particles using

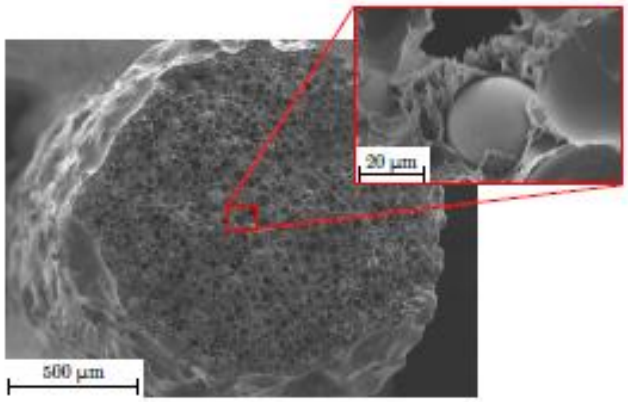

Figure 6.10 SEM micrograph of the Neofer ® 25/60p filament, NdFeB spheres inside the PA11 matrix
Source: Huber, C., C. Abert, F. Bruckner, M. Groenefeld, O. Muthsam, S. Schuschnigg, K. Sirak, R. Thanhoffer, I. Teliban, C. Vogler, R. Windl and D. Suess (2016). "3D print of polymer bonded rare-earth magnets, and 3D magnetic field scanning with an end-user 3D printer." Appl. Phys. Lett. 109(16): 162401.

The printer produced a rectangular magnet with a pyramid notch. This complex geometry is able to minimize the components of the magnetic stray field B in x and y direction in a wide range along the x-axis r_x.; very useful in GMR sensor applications. The printed magnet was magnetized along the z-axis inside a pulse coil with 4 T. The finite element simulation programs called FEMME was used find the optimal design for the magnet by solving magnetostatic Maxwell equations, and using a vector hysteresis model to describe the permanent magnetic material. The illustration below demonstrates the simulation of the rectangular magnet with a pyramid notch and the actual 3D printed object.

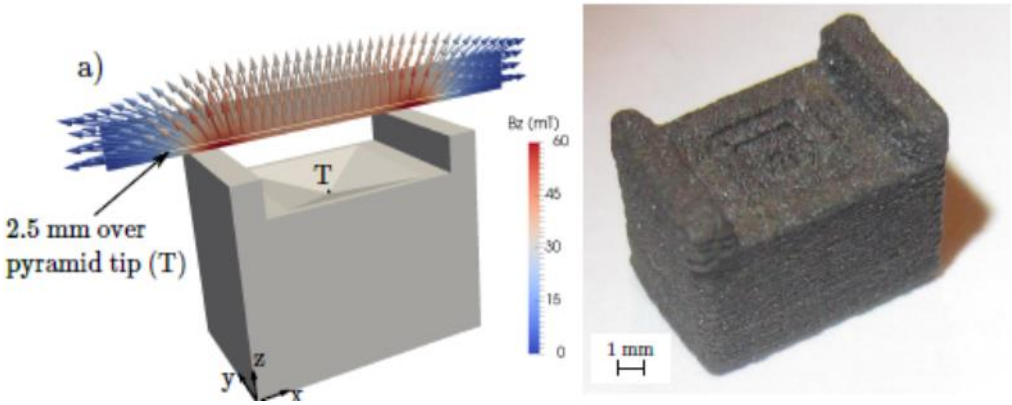

Figure 6.11 1) Geometry of the permanent magnet, and area scan of B with a step size of 0.1mm in the middle of the printed magnet. 2) Printed isotropic NdFeB magnet with Neofer ® 25/60p with optimized shape to suppress B_x and B_y along the x-axis r_x.

Source: Huber, C., C. Abert, F. Bruckner, M. Groenefeld, O. Muthsam, S. Schuschnigg, K. Sirak, R. Thanhoffer, I. Teliban, C. Vogler, R. Windl and D. Suess (2016). "3D print of polymer bonded rare-earth magnets, and 3D magnetic field scanning with an end-user 3D printer." Appl. Phys. Lett. 109(16): 162401.

6.2 Analysis of the Organic Based Magnetic Materials

6.2.1 Analysis of Generation of Neural Radicals

Mahmood et. al. discussed their research of designing organic network structure that generate neutral radicals within the π-conjugated network structure. The figure below shows the self-polymerization synthesized in trifluoromethanesulfonic (TFMSA) acid at 155°C to produce black TCNQ polymer. TFMSA is part of the superacid series that is stronger acid than sulfuric acid, with protonation ability and low nucleophilicity. Trimerization of the cyano (-CN) groups in TCNQ led to the formation of a triazine framework in the presence of TFMSA(Ranganathan, Heisen et al. 2007). The structure consists of a quinone (cyclohexadienedione, $C_6H_4O_2$) moiety surrounded by bulky aromatic triazine (nitrogen-containing heterocycles) rings. The result of this

polymerization was a black product the was soxhlet extracted with methanol and water to wash off any impurities.

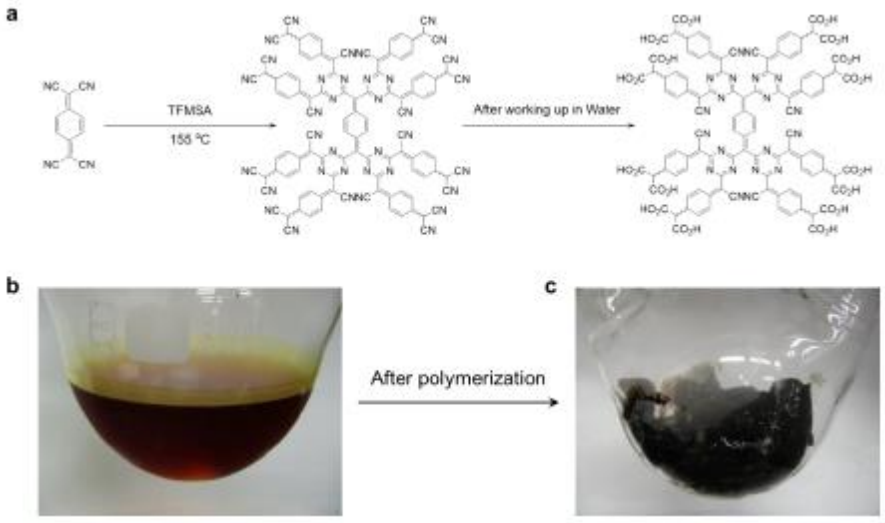

Figure 6.12 (a) Illustration of TCNQ framework with edge groups after aqueous quenching; (b) TCNQ dissolved in TFMSA after stirring at room temperature before self-polymerization; (c) complete gelation of the reaction mixture after polymerization at 155 °C overnight.

Source: Mahmood, J. (2016) "Synthesis of Multifunctional Two-Dimensional Structures and Their Applications", Graduate School of UNIST.

The thermogravimetric analysis (TGA) results, under nitrogen and air environment, show the material over a wide range of temperature has good stability. The powder X-ray diffraction (XRD) pattern exhibited a broad 2θ peak at 24.9, which means the material is amorphous.

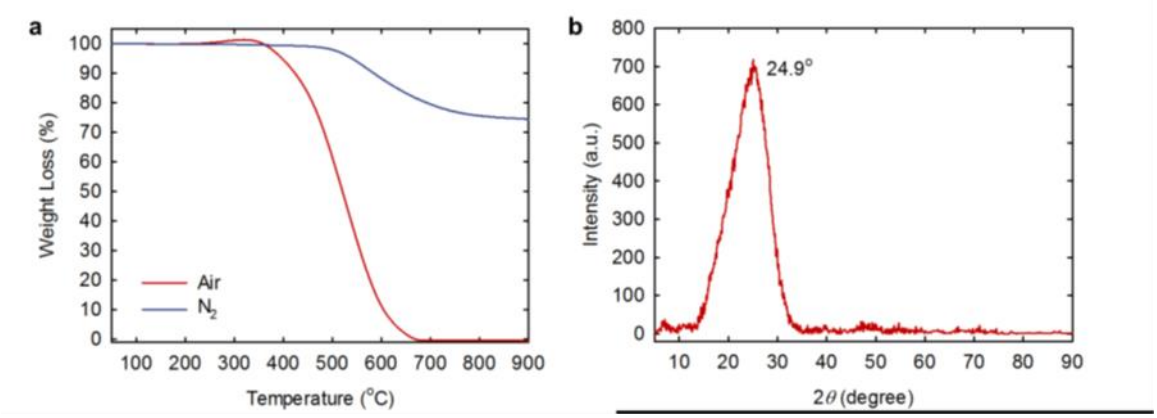

Figure 6.13 a) TGA graph in inert (N2) and air atmosphere b)Powder XRD spectrum exhibiting a broad peak centered at 2θ = 24.9°, implying the amorphous 3D nature of the material.

Source: Mahmood, J. (2016) "Synthesis of Multifunctional Two-Dimensional Structures and Their Applications", Graduate School of UNIST.

The bulk morphology of the p-TCNQ was analyzed with a field-emission scanning electron microscopy (FE-SEM). The images revealed uneven surface texture that consist of grains of irregular shapes and sizes, in the range of several tens of microns in size.

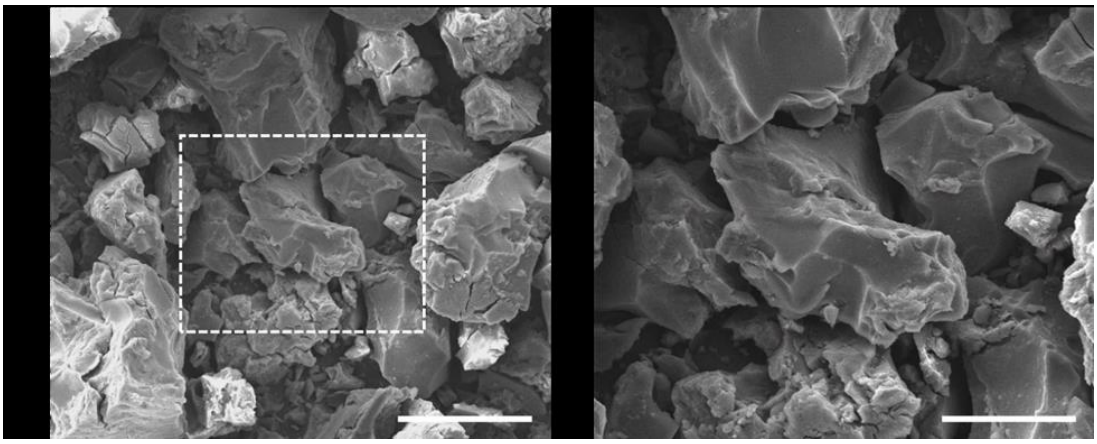

Figure 6.14 SEM images of the p-TCNQ at different magnification showing compact and irregular morphology: a) resolution scale of 100 μm b) Higher resolution scale of 50 μm

Source: Mahmood, J. (2016) "Synthesis of Multifunctional Two-Dimensional Structures and Their Applications", Graduate School of UNIST.

This figure below shows the elemental composition analyzed using X-ray photoelectron spectroscopy (XPS) and elemental analysis (EA) with the results were found to match with theoretical values. Values are shown in the table below.

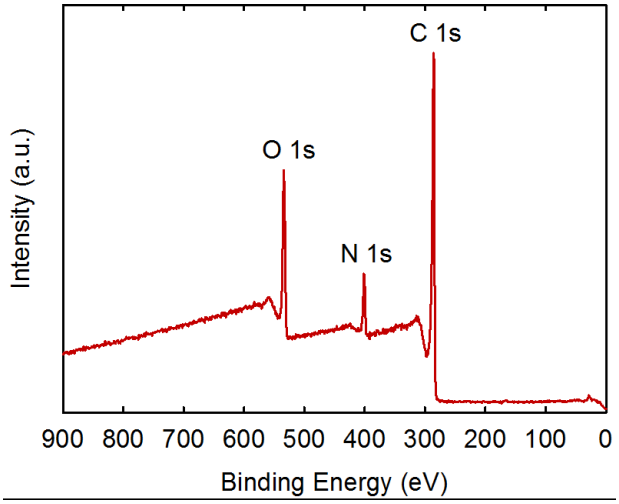

Figure 6.15 XPS survey spectrum from the p-TCNQ.

Source: Mahmood, J. (2016) "Synthesis of Multifunctional Two-Dimensional Structures and Their Applications", Graduate School of UNIST.

Table 4 Elemental composition of the polymerized-TCNQ framework from different characterization techniques

Technique	C	H	N	O	Total
Theoretical (wt.%)	60.57	2.45	13.08	23.91	100
EA (wt.%)	61.42	3	9.57	25.49	99.48
XPS (wt.%)	76.97	----	7.46	15.57	100

Source: Mahmood, J. (2016) "Synthesis of Multifunctional Two-Dimensional Structures and Their Applications", Graduate School of UNIST.

The Solid-state spin electron spin resonance (ESR) spectroscopy confirmed the unpaired electron along the π network using the frequency of 9.5 GHz or "X-band" range at room temperature. This technique delivers short (ns) pulses of microwave radiation to an atom with an unpaired electron and the response of the magnetic field is recorded. X-

band ESR spectrum of polymerized-TCNQ recorded at room temperature, which exhibits a sharp isotropic symmetrical singlet (g = 2.00280) which indicates a carbon free radical (C*). The solid-state NMR spectrum reveals a small broad unusual peak at 40.93 ppm, which is associated with the tertiary radicals in the structure.

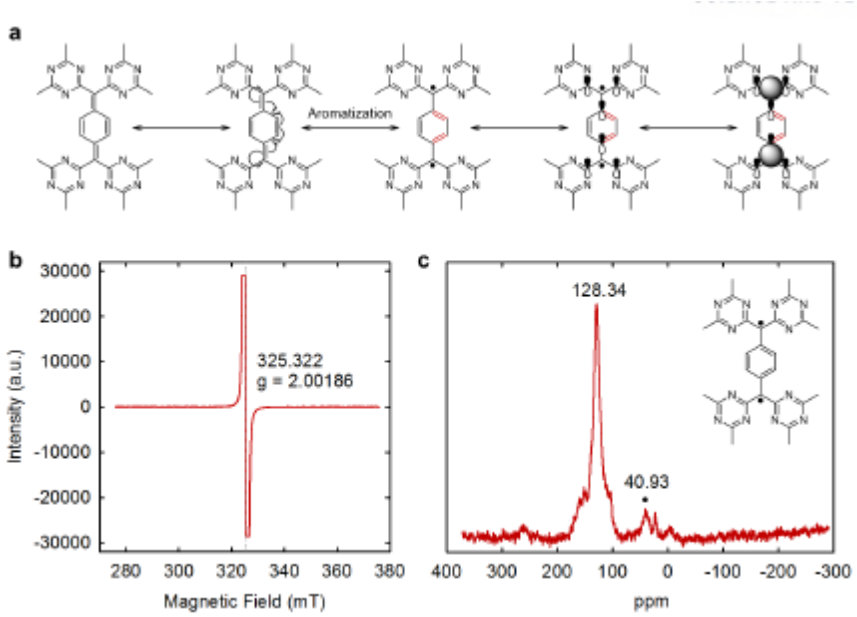

Figure 6.16 (a) Schematic representation of the radical formation and its stability in the structure.; (b) solid-state ESR spectrum of the sample under ambient conditions, showing an isotropic singlet; and (c) solid-state NMR revealing the presence of an unusual peak at 40.93 ppm, which is associated with the tertiary radical in the structure (indicated in the inset by a black dot).

Source: Mahmood, J., J. Park, D. Shin, H.-J. Choi, J.-M. Seo, J.-W. Yoo and J.-B. Baek (2018). "Organic Ferromagnetism: Trapping Spins in the Glassy State of an Organic Network Structure." Chem 4(10): 2357--2369.

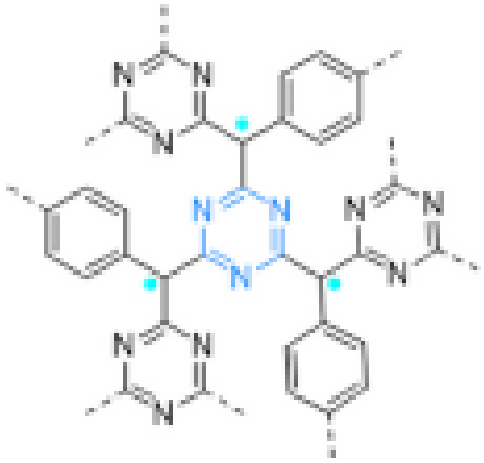

Figure 6.17 Schematic representation of the planar conjugated TCNQ unit with coupled radicals (no spins) shows the local structure around a triazine ring.

Mahmood, J., J. Park, D. Shin, H.-J. Choi, J.-M. Seo, J.-W. Yoo and J.-B. Baek (2018). "Organic Ferromagnetism: Trapping Spins in the Glassy State of an Organic Network Structure." Chem 4(10): 2357--2369

The stability of free radicals at high temperature need two things; kinetic stabilization through the protection of the spin center with a large steric hindrance and thermodynamic stabilization through spin delocalization (resonance). In the self-polymerized TCNQ network structure, the free radicals originate from the aromatization of planar quinone-type cyclohexadiene rings (non-rotatable) into phenyl rings (rotatable), causing the 90° rotation of these phenyl rings. Radicals are present along the connecting carbon atoms in the between the triazine rings and phenyl rings (Fig. 6.18). The generated radicals can be protected by the large steric hindrance in the network structure of p-TCNQ in a glassy state as shown in Fig. 6.19 (Mahmood, Park et al. 2018).

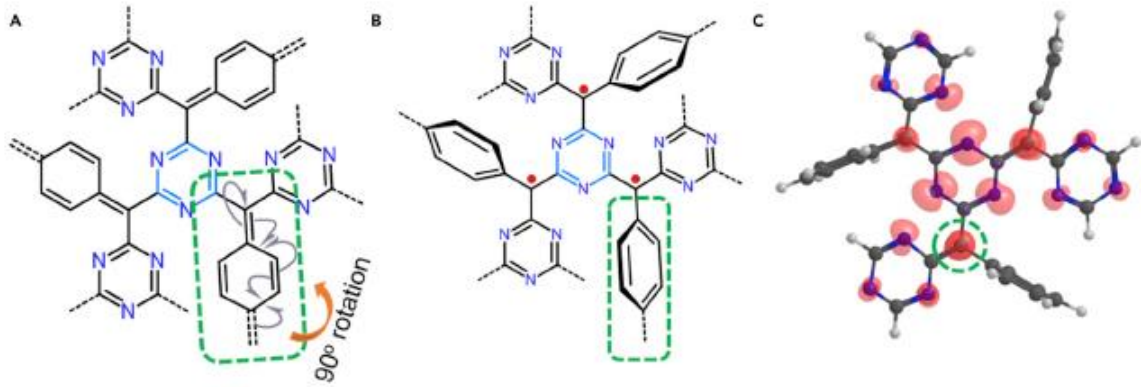

Figure 6.18 (A) Schematic representation of the planar conjugated TCNQ unit with coupled radicals (no spins) shows the local structure around a triazine ring connected by planar quinone-type cyclohexadiene rings (inside dashed green rectangle) (B) The twisted TCNQ unit with radicals (spins) induced by the 90° rotation of phenyl rings, which are formed by the aromatization of quinone-type cyclohexadiene rings (non-rotatable) into phenyl rings (rotatable, indicated inside the dashed green rectangle). Red dots represent the created radicals after rotation. (C) The twisted TCNQ unit with the spin density in the structure (indicated by the green dashed circle) shows the creation of spins on the connecting carbon atoms between the triazine rings and phenyl rings

Source: Mahmood, J., J. Park, D. Shin, H.-J. Choi, J.-M. Seo, J.-W. Yoo and J.-B. Baek (2018). "Organic Ferromagnetism: Trapping Spins in the Glassy State of an Organic Network Structure." Chem 4(10): 2357--2369

Defect structures and their role on the electronic structure of graphite have been essential for the understanding of carbon nanostructures and carbon materials. Defects have profound influence on its electrical, chemical and other physical properties. Recent studies have shown graphene and few-layer graphene have a number of interesting properties.

Atomic force microscopy (AFM), magnetic force microscopy (MFM) and electrostatic force microscopy (EFM) images of the same area on the HOPG surface are shown in Fig. 6.20. The topological image created by AFM reveals a surface with a high population of step edges, surface distortions and defects. The MFM images for b) and c) scan the surface at a height of 50 nm to avoid the long-range van der Waals forces and uncover the magnetic forces. A magnetic signal was detected mostly on the line defects. The lines B and C are grain boundaries of HOPG. Grain boundaries in HOPG are believed

to form a continuous network over graphite surface; interconnect with each other. EFM analysis was measured on the same place with Pt coated Si tip with a lift scan height of 20 nm. A bright contrast is observed on the same places as in the MFM images.

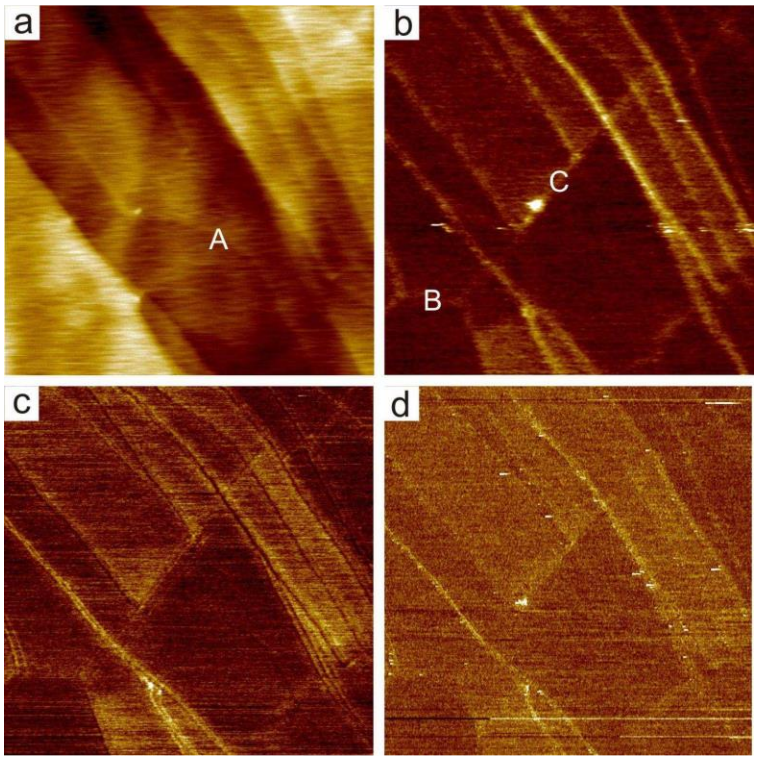

Figure 6.19 The same area on the HOPG surface imaged with AFM (a), MFM (b) and (c), and EFM (d). MFM tip has been magnetized into the graphite surface (b) and out of the graphite surface (c), respectively

Source: Cervenka, J., M. I. Katsnelson and C. F. J. Flipse (2009). "Room-temperature ferromagnetism in graphite driven by two-dimensional networks of point defects." Nat. Phys. 5(11): 840--844.

Graphite surface have been for a long time characterized by scanning tunneling microscope (STM), however defect structure is not well understood especially in the sp^2 bonded carbon lattice. The STM images shown in Fig. 6.21 are one-dimensional superlattices with a height corrugation up to 1.5 nm due to a charge accumulation

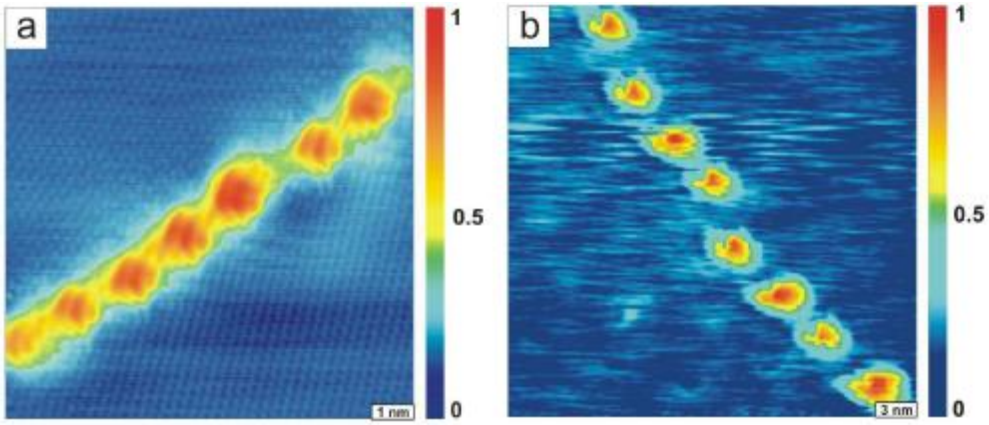

Figure 6.20 STM image of a grain boundary on HOPG showing a 1D superlattice with a small periodicity D = 1.4 nm (a) and a large periodicity D = 4 nm (b).

Source: Cervenka, J., M. I. Katsnelson and C. F. J. Flipse (2009). "Room-temperature ferromagnetism in graphite driven by two-dimensional networks of point defects." Nat. Phys. 5(11): 840--844.

In Fig. 6.22, the STM images and STS spectra are basically showing two typical grain boundaries with different periodicities. STS on grain boundaries exhibits localized electron states that are not present on the bare graphite surface. The grain boundaries was between defect < 4 nm was characterized two split localized electron states, while grain boundaries with large distances between their defects > 4 nm display only one localized state, similarly like solitary defects in graphite (Červenka, Katsnelson et al. 2009). This may prove the origin of ferromagnetism.

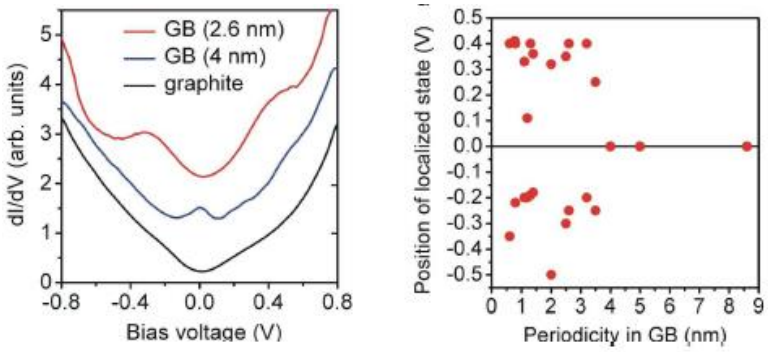

Figure 6.21 On the right, STS on two grain boundaries and on the bare graphite surface

Source: Cervenka, J., M. I. Katsnelson and C. F. J. Flipse (2009). "Room-temperature ferromagnetism in graphite driven by two-dimensional networks of point defects." Nat. Phys. 5(11): 840--844.

6.2.2 Analysis of Ferromagnetic Ordering

In order to have stable organic ferromagnetic material at room temperature, there must be at the microscale level highly stable spin trapping at glassy state and ferromagnetic ordering among the spin centers. Depending on the concentration of the spin centers, the presence of these radicals creates long-range magnetic order through the π-conjugated network. The magnetic properties of the TCNQ framework were characterized using a Quantum Design SQUID-VSM. The background diamagnetic signal was subtracted from all magnetic data Fig. 6.23.

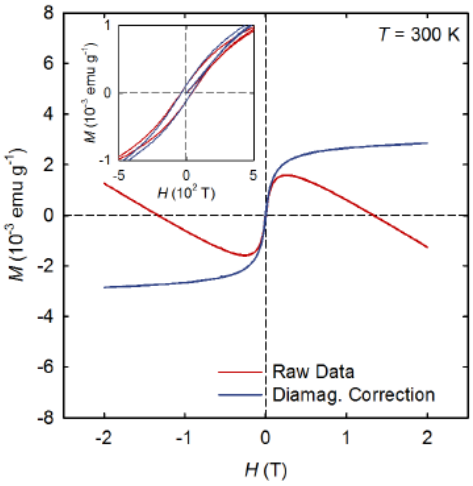

Figure 6.22 Magnetization as a function of field recorded at 300 K. Dark red line represent the raw experimental data of magnetization. Dark blue line represents the magnetization after subtracting linear diamagnetic background.

Source: Mahmood, J. (2016) "Synthesis of Multifunctional Two-Dimensional Structures and Their Applications", Graduate School of UNIST.

The next figure illustrates the field-dependent magnetization of samples recorded at 5 K and 300 K. The sample clearly show spontaneous magnetization with distinctive hysteresis was clearly observed even at 300 K, with non-zero coercivity

and remanence (Cervenka, Katsnelson et al. 2009). The stability of the sample's the magnetic moment was measured after N_2 atmosphere storage for about three weeks with no noticeable degradation.

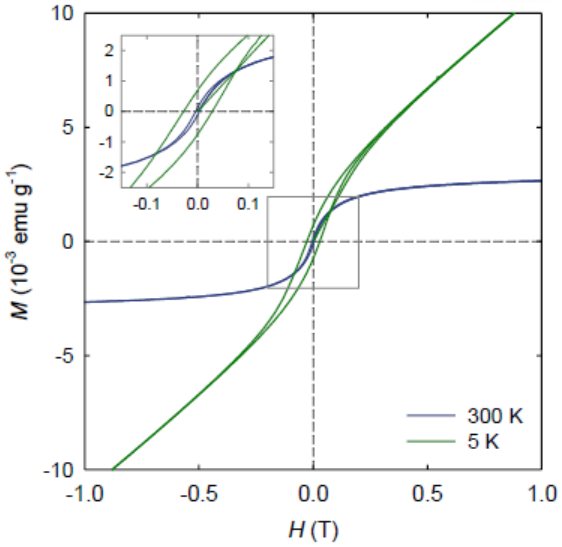

Figure 6.23 Magnetization as a function of the applied field (H), recorded at 300 K and 5 K with the diamagnetic background subtracted from all data. The material possesses spontaneous magnetization, even at 300 K. Closer view of the hysteresis loop is shown in the inset.

Source: Mahmood, J., J. Park, D. Shin, H.-J. Choi, J.-M. Seo, J.-W. Yoo and J.-B. Baek (2018). "Organic Ferromagnetism: Trapping Spins in the Glassy State of an Organic Network Structure." Chem 4(10): 2357--2369.

The temperature dependence of the field-cooled (FC) and zero-field-cooled (ZFC) magnetization with H = 1,000 Oe (Fig. 6.25). ZFC magnetizations were recorded after cooling of the sample in the absence of the magnetic field, while FC magnetizations were recorded after cooling of the sample in the applied magnetic field. The TCNQ have a Curie temperature was Tc = ~ 495 K which means the material demonstrate "spin-glass" behavior due to the high temperature transition. Magnetization as a function of $\mu_B H/k_B T$ for various temperatures cyan line represents a fit to the Brillouin function with J = S = 1/2 under the

assumption of g = 2. The Brillouin function provides good fits only when J = S = 1/2 (free electron spin).

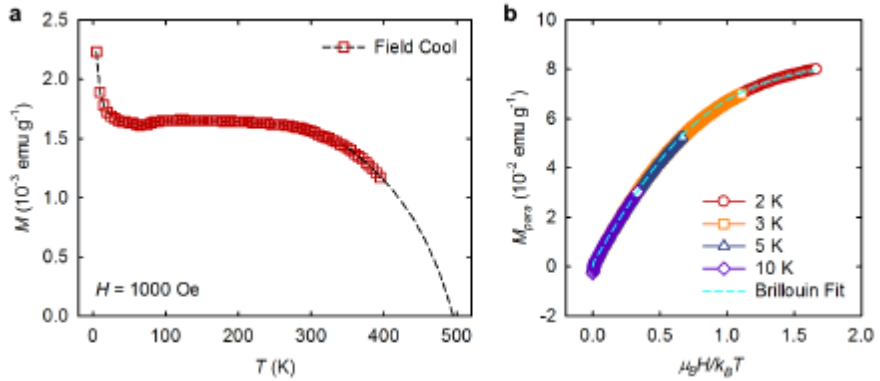

Figure 6.24 Magnetization as a function of the temperature, recorded at 1000 Oe. Robust spontaneous magnetization persists up to 400 K. The estimated critical temperature is Tc ~ 495 K (b) magnetization as a function of $\mu_B H/kBT$ at various temperatures

Source: Mahmood, J., J. Park, D. Shin, H.-J. Choi, J.-M. Seo, J.-W. Yoo and J.-B. Baek (2018). "Organic Ferromagnetism: Trapping Spins in the Glassy State of an Organic Network Structure." Chem 4(10): 2357--2369.

Down below are more example of the application of the Brillion function to figure out the angular momentum quantum number J.

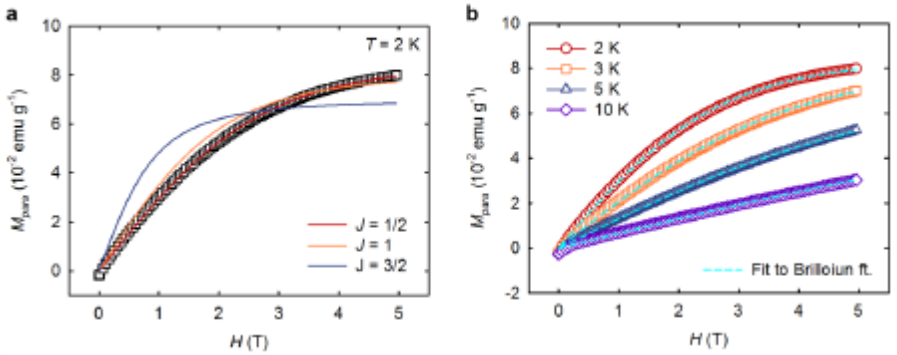

Figure 6.25 Determination of the angular momentum quantum number J via Brillouin function fit.

Source: Mahmood, J., J. Park, D. Shin, H.-J. Choi, J.-M. Seo, J.-W. Yoo and J.-B. Baek (2018). "Organic Ferromagnetism: Trapping Spins in the Glassy State of an Organic Network Structure." Chem 4(10): 2357--2369.

Fig. 6.26 shows the SQUID magnetization measurements on HOPG after subtraction of the diamagnetic signals at 5 K and 300 K. Detection of the magnetic signal of the HOPG

requires an interesting setup, with the MFM tip magnetized in two opposite directions by pointing into and out of the graphite surface plane. MFM signal represents the phase shift between the probe oscillation and the driving signal due to magnetic force acting on the tip, the dependence of the phase shift on the force gradient can be expressed by a simple form(Kebe and Carl 2004):

$$\Delta\Phi = \frac{Q}{k}\frac{\partial F}{\partial z} \tag{20}$$

Where Q is quality factor and k is spring constant of the cantilever. With this equation, qualitative analysis can be conducted, where a positive phase shift (bright contrast) represents a repulsive force between the tip and the sample, and a negative phase shift (dark contrast) manifests an attractive interaction relative to the background signal. When the defect's net magnetic moment orientation stays the same direction, this means that some form of ferromagnetic order is occurring at the defect sites at room temperature. Fig. 6.2 down below show the models of two basics shapes of grain boundaries in graphite

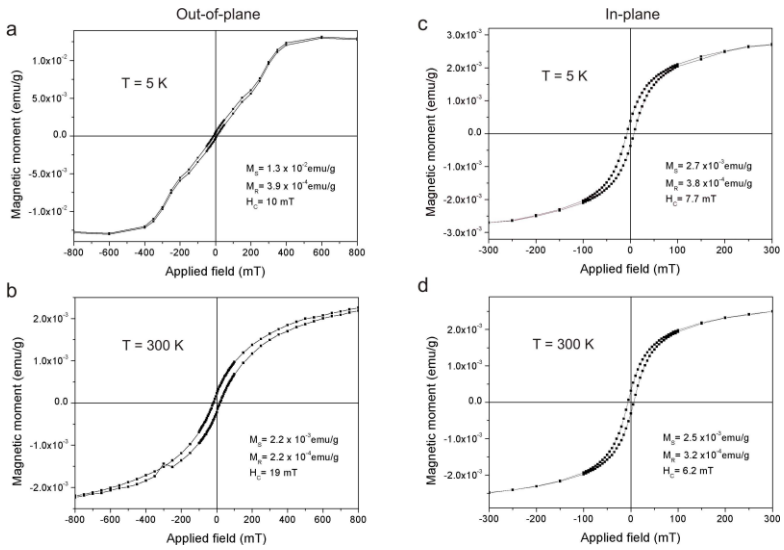

Figure 6.26 Out-of plane (a,b) and in-plane (c,d) SQUID magnetization measurements on HOPG after subtraction of the diamagnetic signals at 5 K and 300 K. Magnetic field has been applied along the c axis in the out-of-plane direction and along the graphene planes in the in-plane direction.

Source: Mahmood, J., J. Park, D. Shin, H.-J. Choi, J.-M. Seo, J.-W. Yoo and J.-B. Baek (2018). "Organic Ferromagnetism: Trapping Spins in the Glassy State of an Organic Network Structure." Chem 4(10): 2357--2369.

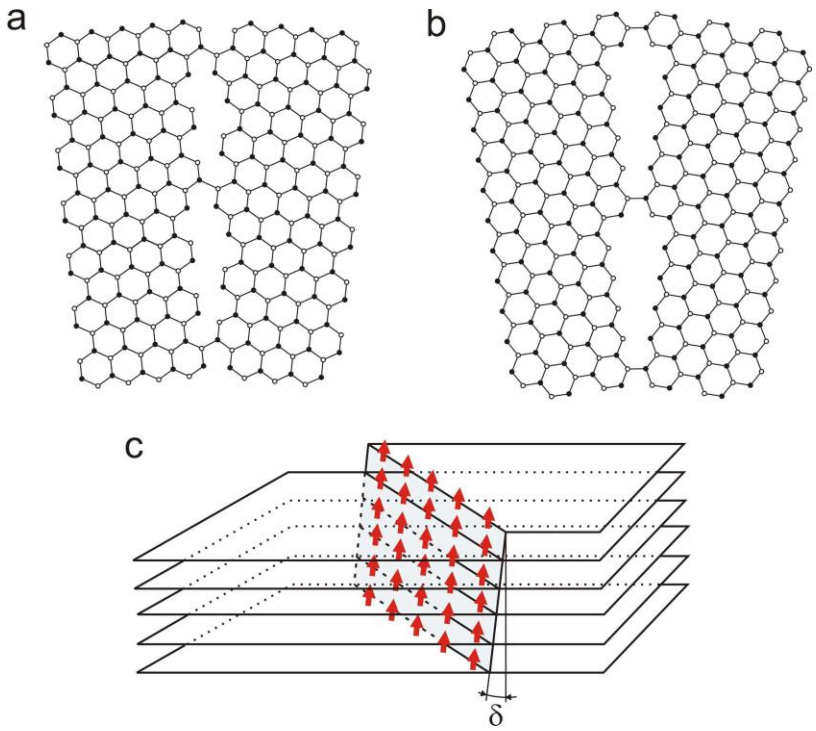

Figure 6.27 Models of two basics shapes of grain boundaries in graphite: (a) armchair direction with periodicity D and (b) zigzag direction with periodicity 3D. (c) 2D in-plane magnetized grain boundary propagating through bulk HOPG.

Source: Mahmood, J., J. Park, D. Shin, H.-J. Choi, J.-M. Seo, J.-W. Yoo and J.-B. Baek (2018). "Organic Ferromagnetism: Trapping Spins in the Glassy State of an Organic Network Structure." Chem 4(10): 2357--2369.

6.2.3 Analysis of Metal Contamination

It is important to prove that the origin of the organic material's ferromagnetism was not due to any possible metal contamination The HOPG samples were analyzed for impurity concentration using the particle induced X-ray emission (PIXE) in the bulk material and by low energy ion scattering (LEIS) at the surface. The PIXE was found Fe with concentration ≈ 20 mg/g and other magnetic and metallic impurities at levels below 1 mg/g. The measured content of Fe impurities in HOPG is not sufficient to produce the

ferromagnetic signal. The surface analysis by LEIS has not detected any magnetic elements indicating impurity concentration below 100 ppm. For the polymerized-TCNQ, the inductively coupled plasma mass spectrometry was applied to identify any trace metal contents in the material. The results are summarized in the table below.

Table 5 Trace metal analysis of the impurities in the p-TCNQ framework determined by ICP-MS

Element	Mg	Al	V	Cr	Mn	Fe	Co
Concentration (ppm)	0.00306	0.0039	0.00672	0.00401	0.000121	0.00619	0.0242
Element	**Ni**	**Cd**	**In**	**Pb**	**B**	**Ti**	**Zr**
Concentration (ppm)	0.000288	0.0237	0.00514	0.00014	0.0894	0.0326	0.00132

Source: Mahmood, J., J. Park, D. Shin, H.-J. Choi, J.-M. Seo, J.-W. Yoo and J.-B. Baek (2018). "Organic Ferromagnetism: Trapping Spins in the Glassy State of an Organic Network Structure." Chem 4(10): 2357--2369.

6.3 3D Printing of Organic Based Magnetic Materials

There were only a few papers out there that have attempted to the print organic based material. The main reason is the difficulty of producing stable molecular/organic system that display ferromagnetic ordering at room temperature. Even after the reproducible success of magnetic material, it will have to sustain its properties through the printing process. Wei, Li et al. conducted the preparation of 3D Printable Graphene Composite with graphene loading up to 7.4 wt% to usher in a new type of composite filament. The graphene fillers can be replaced with HOPG fillers in the attempt to new type of magnetic filament.

SEM provided surface analysis on the graphene individuals captured within the polymer matrix with different contrast and detailed morphologies. The images were taken from both the surface and the cross section of the composite study the overall graphene

dispersion inside the composites. Graphene sheets, with lateral size around 3–5 μm, represent the bright sheets that are lightly scatter in the dark polymer context. As the graphene loading increase a continuous and denser graphene network develop within the polymer matrix. Aggregations of the graphene sheets was observed in the 7.4 wt% Graphene-ABS sample, which can cause 3D printing's nozzle jam.

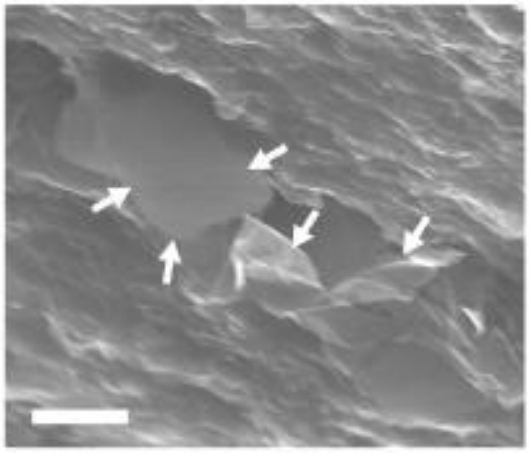

Figure 6.28 Cross-section SEM image of 3.8 wt.% G-ABS composite showing the partially incorporated graphene sheets.

Source: Wei, X., D. Li, W. Jiang, Z. Gu, X. Wang, Z. Zhang and Z. Sun (2015). "3D Printable Graphene Composite." Sci. Rep. 5: 11181.

A laser excitation with a wavelength of 785 nm was applied to the samples and record as the Raman spectra. The spectrum for the G-ABS (3.8 wt% graphene loading) shows a broad D peak at ~1330 cm^{-1} and a G peak at ~1600 cm^{-1}, which is related to the defects and sp^2 structures in graphene. A relative weak peak at ~2240 cm^{-1} can be attributed to the C≡N stretch in ABS (Foster, Down et al. 2017).

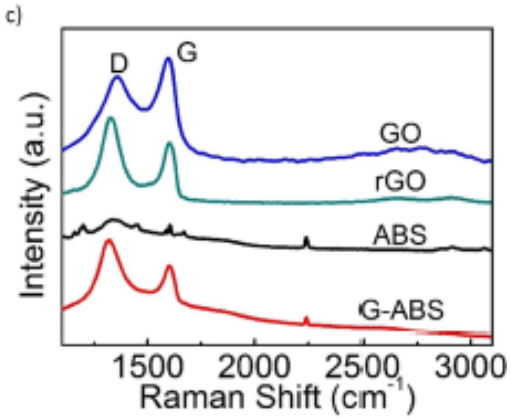

Figure 6.29 Raman spectra in prepared GO, rGO, ABS and G-ABS samples.

Source: Wei, X., D. Li, W. Jiang, Z. Gu, X. Wang, Z. Zhang and Z. Sun (2015). "3D Printable Graphene Composite." Sci. Rep. 5: 11181.

UV-vis spectrum of the graphene oxide (GO) confirmed characteristic absorption at ~231 nm, corresponding to the π -π * transition in GO. After chemical reduction with hydrazine the peak shift over to ~265 nm, representing the restoration of the conjugated structure in reduced GO. The same peak at ~265 nm can be seen in the UV-vis spectrum for standard graphene-ABS samples show what sample would look like when the GO is completely reduced.

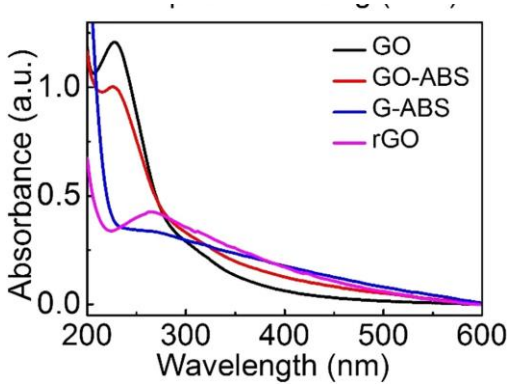

Figure 6.30 UV-vis spectra of separated samples dispersed in aqueous solutions, including GO, GO-ABS, G-ABS, rGO.

Source: Wei, X., D. Li, W. Jiang, Z. Gu, X. Wang, Z. Zhang and Z. Sun (2015). "3D Printable Graphene Composite." Sci. Rep. 5: 11181.

Temperatures of nozzle, heated build chamber and heated build platform are crucial parameters to smoothly print the composite filament. The calibration of the 3D printing system for optimal printing performance requires the filament samples' thermal and mechanical properties were carefully assessed with standard techniques, such as differential scanning calorimetry (DSC), dynamic mechanical analysis (DMA), thermogravimetric analysis (TGA) and thermomechanical analysis (TMA).

The first step, before any 3D printing, is to find the materials' vital parameter, the glass transition temperature (T_g), which was determined from the DSC curves (Fig. 6.31). The pure ABS have a T_g value close to ~105.8 °C with the value shifting slightly to ~110 °C with incremental graphene loadings. This due to the graphene network developing with the polymer matrix adding reinforcements. The graphene sheet material also restricts the segmental mobility of ABS's chain segments near graphene sheets, which increases the melting temperature of the amorphous materials. The DMA-derived Tg values also show agreement as the graphene loading increases.

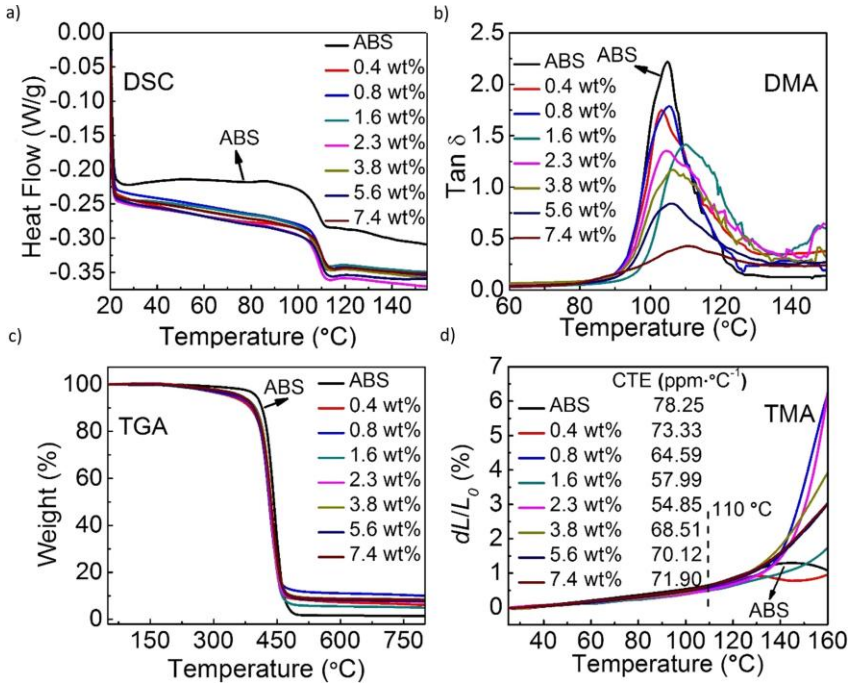

Figure 6.31 Thermal and mechanical analysis of ABS and G-ABS composites.

Source: Wei, X., D. Li, W. Jiang, Z. Gu, X. Wang, Z. Zhang and Z. Sun (2015). "3D Printable Graphene Composite." Sci. Rep. 5: 11181.

Huang et al. developed an additive manufacturing method for a cobalt-based organic ferromagnetic material. The material is identified as $Co(tpy)Cl_2 \cdot MeCN$ in formula and a magnetic moment of 0.24 emu/g and a coercivity of about 50 Oe as shown in the magnetization loop below.

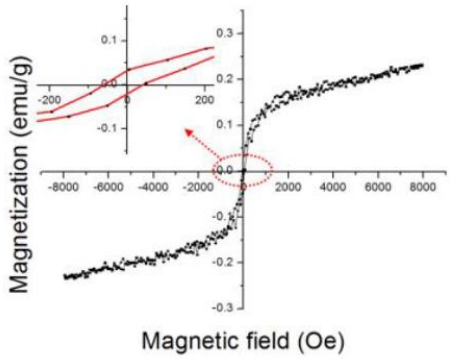

Figure 6.32 Magnetization loop at room temperature for cobalt-based organic compound, Hc= 50 Oe.

Source: Huang, J., K. C. Yung, Z. Meng, D. T. C. Ang and G. Li (2017). "Additive manufacturing of Cobalt-based Organic Ferromagnetic Materials." IEEE Magn. Lett. PP(99): 1.

The $Co(tpy)Cl_2 \cdot MeCN$ nanoparticles were printed onto glass and silicon wafer using the same parameters. To investigate the substrate influence and droplet spacing, optical microscopy was applied. Image a) shows the multi-line shape patterns with 80 μm droplet spacing while image b) shows line shape pattern with 110 μm distance. The contact angles of the ink, caused by the influence of the substrate, were measured to be 17.6° for glass and 16.2° for silicon wafer. For c) and d), the width of printed pattern in line shape was around 513 μm on the glass slides and 804 μm on the silicon wafer, respectively.

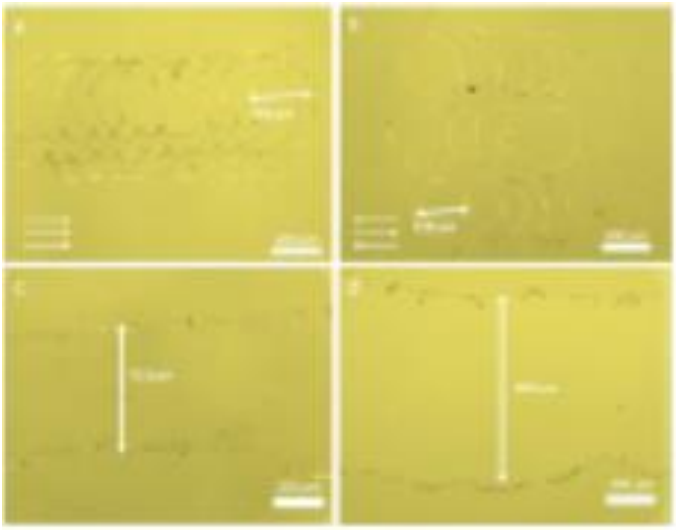

Figure 6.33 (a) Optical microscopy image of multi-line shape pattern with 80 μm spacing distance. (b) Optical microscopy image of line shape pattern with 110 μm spacing distance. (c) Optical microscopy image of one-line pattern on the glass slide. (d) Optical microscopy image of one-line pattern on the silicon wafer.

Source: Huang, J., K. C. Yung, Z. Meng, D. T. C. Ang and G. Li (2017). "Additive manufacturing of Cobalt-based Organic Ferromagnetic Materials." IEEE Magn. Lett. PP(99): 1.

SEM images down below show the micro structures of the printed patterns. The images a) and b) presented the printed patterns in same condition on glass and on silicon wafer. Cuboid structures were detected on the substrate with length ranging from 300 nm to 3 μm at the long sides due to material distribution, decreasing from edge to center similar

to coffee-ring effects. This material distributions are shown more intensively and clearly in a) compared to b) caused by lower spreading ratio and poor quality of surface This is why the silicon wafer was the substrate used for fabricating the 2.5D printed pattern.

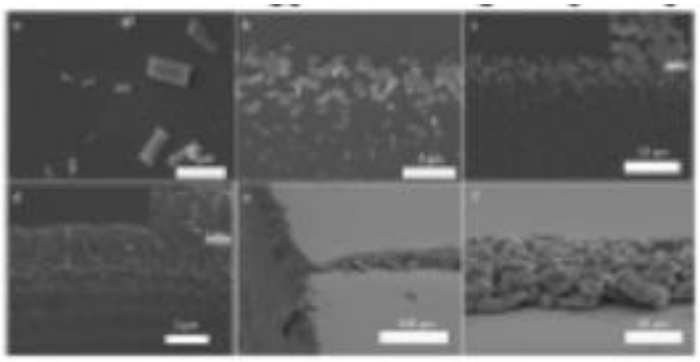

Figure 6.34 a) SEM image of particle on the glass slide. (b) SEM image of particle on the silicon wafer. (c) SEM image of one-line pattern at the edge in one-time printing. Inset is enlarged image. (d) SEM image of one-line pattern at the edge in ten-time printing. Inset is enlarged image. (e) SEM image of multi-line pattern in a 15-degree angle view in macroscopic aspect. (f) Magnified SEM image of multi-line pattern in a 15-degree angle view

Source: Huang, J., K. C. Yung, Z. Meng, D. T. C. Ang and G. Li (2017). "Additive manufacturing of Cobalt-based Organic Ferromagnetic Materials." IEEE Magn. Lett. PP(99): 1.

The morphology and magnetic topography of the nanoparticles were studied via AFM and MFM. Fig. 6.36 a) showed topography image for cobalt-based ferromagnetic nanoparticle and Fig. 6.36 b) the magnetic phase image. The topographical image shows the particles distribution with few overlapping. The magnetic contrast in MFM image is related to the topographic bright and dark areas. The particles are forming these agglomerated circle-shape samples revealed extremely high brightness with almost 300 nm height with the MFM image revealing a magnetic contrast at the same location. The magnetic contrast in MFM image matches with the morphology in the corresponding AFM image, which demonstrate the printed samples' strong magnetic signal.

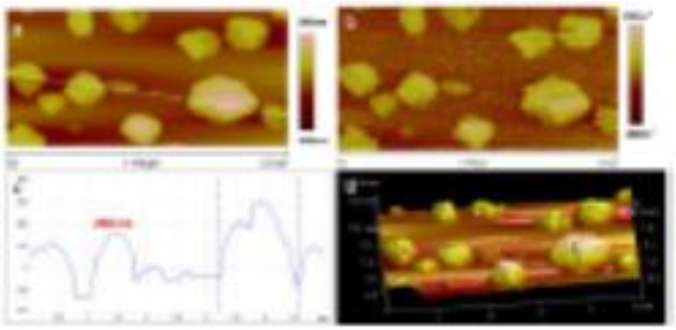

Figure 6.35 (a) AFM image of the printed crystals. (b) Corresponding MFM image. (c) The corresponding AFM height profile. (d) 3D view of AFM image.

Source: Huang, J., K. C. Yung, Z. Meng, D. T. C. Ang and G. Li (2017). "Additive manufacturing of Cobalt-based Organic Ferromagnetic Materials." IEEE Magn. Lett. PP(99): 1.

CHAPTER 7

CONCLUSION

Additive manufacturing of NdFeB bonded materials has a promising future in various technological fields. Ortner, Huber et al. have applied their previous works to the improvement of 1D magnetic position and orientation systems using a 3D printer. Using topology optimization methods to find predefined geometric parameters and fabricate magnetic materials with specific magnetic field shape will have a significant impact. AM technology will allow magnetic components to be tested in early prototyping stages and minimizing manufacturing/processing wastes while using smaller quantities of the rare earth materials

Organic based magnets are emerging class of new materials that feature properties which include low-density, transparency, electrical insulation, low temperature fabrication, as well as combining magnetic ordering with other properties such as photo responses. Most of its common magnetic properties are comparable to the conventional metal and rare earth-based magnets. The next big challenge for scientists is to create many new high-spin molecules that possess energy gaps, an order of magnitude greater, at room temperature as well as kinetic stability that rivals the most stable organic monoradicals.

Induced magnetism in HOPG will open new research in magnetism in many applications such as spin electronics. Enhancing the properties of the hydrogen-induced ferrimagnetism in HOPG will create interesting applications such as producing the smallest controlled magnet ever possible. The demonstration of the self-polymerization of TCNQ, using a simple low-temperature processing to fabricate metal-free polymeric organic

magnet with magnetic ordering at RT is very promising. Understanding and creating new well-defined bulky molecular framework that protects radicals with the large steric hindrance and manipulating the spins in polymeric organic networks allows alternative approaches for versatile future applications of plastic magnets. Combining the development of organic based magnets with AM methods will further bring new and interesting innovation to the technological world we live in.

REFERENCES

Acker, D. S. and W. R. Hertler (1962). "Substituted Quinodimethans. I. Preparation and Chemistry of 7,7,8,8-Tetracyanoquinodimethan." J. Am. Chem. Soc. **84**(17): 3370--3374.

Anderson, J. J. (2010). "Structural and Magnetic Properties of NdFeB Cluster." Mechanical (and Materials) Engineering -- Dissertations, Theses, and Student Research.: 64.

Aoki, Y., Y. Orimoto and A. Imamura (2017). Quantum Chemical Approach for Organic Ferromagnetic Material Design | SpringerLink, Springer, Cham.

Bates, E. M., W. J. Birmingham and C. A. Romero-Talamas (2015). "Development of a Bitter-Type Magnet System." IEEE Trans. Plasma Sci.: 1--5.

Blundell, S. and D. Thouless (2003). Magnetism in Condensed Matter.

Borden, W. T., E. R. Davidson and P. Hart (1978). "The potential surfaces for the lowest singlet and triplet states of cyclobutadiene." J. Am. Chem. Soc. **100**(2): 388--392.

Capelle, K. (2002). "A bird's-eye view of density-functional theory." Braz. J. Phys **36**(4).
Červenka, J. and C. F. J. Flipse (2009). "Structural and electronic properties of grain boundaries in graphite: Planes of periodically distributed point defects." Phys. Rev. B **79**(19): 195429.

Cervenka, J., M. I. Katsnelson and C. F. J. Flipse (2009). "Room-temperature ferromagnetism in graphite driven by two-dimensional networks of point defects." Nat. Phys. **5**(11): 840--844.

Červenka, J., M. I. Katsnelson and C. F. J. Flipse (2009). "Room-temperature ferromagnetism in graphite driven by two-dimensional networks of point defects." Nat. Phys. **5**(11): 840.

Coey, J. M. D. (2010). "Magnetism and Magnetic Materials by J. M. D. Coey." Cambridge Core.

Coey, J. M. D. (2011). "Hard Magnetic Materials: A Perspective." Magnetics, IEEE Transactions on **47**(12): 4671--4681.

Foster, C. W., M. P. Down, Y. Zhang, X. Ji, S. J. Rowley-Neale, G. C. Smith, P. J. Kelly and C. E. Banks (2017). "3D Printed Graphene Based Energy Storage Devices." Sci. Rep. **7**: 42233.

Gallagher, N. M., A. Olankitwanit and A. Rajca (2015). "High-Spin Organic Molecules." J. Org. Chem. **80**(3): 1291--1298.

Grössinger, R. (2008). "Characterisation of hard magnetic materials." ResearchGate **59**(7): 15--20.
Guo, N. and M. C. Leu (2013). "Additive manufacturing: technology, applications and research needs." Frontiers of Mechanical Engineering **8**(3): 215-243.

Gutfleisch, O., M. A. Willard, E. Bruck, C. H. Chen, S. G. Sankar and J. P. Liu (2011). "Magnetic materials and devices for the 21st century: stronger, lighter, and more energy efficient." Adv Mater **23**(7): 821-842.

Herbst, J. F., J. J. Croat, F. E. Pinkerton and W. B. Yelon (1984). "Relationships between crystal structure and magnetic properties in Nd2Fe14B." Physical Review B **29**(7): 4176-4178.

Huang, J., K. C. Yung, Z. Meng, D. T. C. Ang and G. Li (2017). "Additive manufacturing of Cobalt-based Organic Ferromagnetic Materials." IEEE Magn. Lett. **PP**(99): 1.

Huber, C., C. Abert, F. Bruckner, M. Groenefeld, O. Muthsam, S. Schuschnigg, K. Sirak, R. Thanhoffer, I. Teliban, C. Vogler, R. Windl and D. Suess (2016). "3D print of polymer bonded rare-earth magnets, and 3D magnetic field scanning with an end-user 3D printer." Appl. Phys. Lett. **109**(16): 162401.

Jimenez-Villacorta, F. and L. H. Lewis (2014). "“Advanced Permanent Magnetic Materials”." ResearchGate: 30.

Kasisomayajula, V., M. Booty, A. T. Fiory and N. M. Ravindra (2012). "Magnetic Field Assisted Heterogeneous Device Assembly." John Wiley & Sons, Ltd: 651--661.

Kebe, T. and A. Carl (2004). "Calibration of magnetic force microscopy tips by using nanoscale current-carrying parallel wires." J. Appl. Phys. **95**(3): 775--792.

Lewis, J. A. (2006). "Direct Ink Writing of 3D Functional Materials." Adv. Funct. Mater. **16**(17): 2193--2204.

Mahmood, J. Synthesis of Multifunctional Two-Dimensional Structures and Their Applications, Graduate School of UNIST.

Mahmood, J., J. Park, D. Shin, H.-J. Choi, J.-M. Seo, J.-W. Yoo and J.-B. Baek (2018). "Organic Ferromagnetism: Trapping Spins in the Glassy State of an Organic Network Structure." Chem **4**(10): 2357--2369.

Marini, D., D. Cunningham and J. R. Corney (2017). "Near net shape manufacturing of metal: A review of approaches and their evolutions." Proceedings of the Institution of Mechanical Engineers, Part B: Journal of Engineering Manufacture **232**(4): 650--669.

Pickard, C. J. and F. Mauri (2002). "First-Principles Theory of the EPR g Tensor in Solids: Defects in Quartz." Phys. Rev. Lett. **88**(8): 086403.

Ranganathan, A., B. C. Heisen, I. Dix and F. Meyer (2007). "A triazine-based three-directional rigid-rod tecton forms a novel 1D channel structure." Chem. Commun. (Camb). **35**: 3637--3639.

Rombouts, M., J. P. Kruth, L. Froyen, J. Van Vaerenbergh and P. Mercelis (2005). "Binding mechanisms in selective laser sintering and selective laser melting." Rapid Prototyping Journal **11**(1): 26-36.

Satoshi Hirosawa, M. N., and Seiji Miyashita (2017). "Perspectives for high-performance permanent magnets: applications, coercivity, and new materials." Advances in Natural Sciences: Nanoscience and Nanotechnology **8**.

Skomski, R. and J. M. D. Coey (2016). "Magnetic anisotropy — How much is enough for a permanent magnet?" Scr. Mater. **112**: 3--8.

Van Vleck, J. H. (1978). "Quantum Mechanics: The Key to Understanding Magnetism." Science **201**(4351): 113--120.

Virjoghe, E. O., D. Enescu, M.-F. Stan and M. Ionel (2012). "Finite Element Analysis of Stationary Magnetic Field." IntechOpen.

Wang, X., M. Jiang, Z. Zhou, J. Gou and D. Hui (2017). "3D printing of polymer matrix composites: A review and prospective." Composites Part B **110**: 442--458.

Xiao, J. and J. U. Otaigbe (2000). "Polymer bonded magnets. II. Effect of liquid crystal polymer and surface modification on magneto-mechanical properties." Polym. Compos. **21**(2): 332--342.